Arabian Journal of Chemistry (2023) **16**, 104679

King Saud University

Arabian Journal of Chemistry

www.ksu.edu.sa
www.sciencedirect.com

ORIGINAL ARTICLE

Preparation of polyprenol/poly (β-amino ester)/galactose targeted micelle carrier for enhancing cancer therapy

Hua Yuan [a], Changwei Zhang [a,b,c,*], Peng Zhou [d], Xiaoran Yang [a], Ran Tao [a,b,c], Jianzhong Ye [a,b,c], Chengzhang Wang [a,b,c,*]

[a] *Institute of Chemical Industry of Forest Products, CAF, Nanjing 210042, Jiangsu, China*
[b] *Institute of Ecological Conservation and Restoration, CAF, Beijing, l00091, China*
[c] *Co-Innovation Center of Efficient Processing and Utilization of Forest Resources, Nanjing Forestry University, Nanjing 210042, Jiangsu, China*
[d] *College of Materials Science and Engineering, Central South University of Forestry and Technology, Changsha 410004, Hunan, China*

Received 4 December 2022; accepted 11 February 2023
Available online 21 February 2023

KEYWORDS

Ginkgo biloba leaves;
Polyprenol;
Target;
Carrier;
Cancer

Abstract Lacking of substantial physiological activity and low utilization remains a problem for most conventional drug carriers. Polyprenol with beneficial medical effects and high availability could be an ideal candidate for solving this issue. Here, Ginkgo biloba leaves polyprenol (GBP)-based derivative was prepared by Michael addition reaction of poly (β-amino esters) (PBAE) with GBP and galactose (Gal). The intervention of poly (β-amino ester) and galactose promoted GBP-PBAE-Gal to depict as micellar carrier, enhancing the loading of hydrophobic DOX and the sensitivity to the specific tumor microenvironment, with the largest DOX loading of 28.62 ± 1.49 % and the efficient DOX release rate of 90.30 %. In the meantime, GBP-PBAE-Gal exhibited enhanced colloidal stability at 640-folds of dilution and in the presence of serum and realized the possibility of long-term storage at room temperature. Additionally, GBP-PBAE-Gal was safe for human red blood cells and human normal liver cells HL-7702. When applied for DOX delivery to HepG2 cells, GBP-PBAE-Gal increased the targeting of DOX to intensify its inhibition on HepG2 cells. Compared to free DOX, the DOX loaded into GBP-PBAE-Gal presented stronger

* Corresponding authors.
E-mail addresses: zhangcwlhs@sina.com (C. Zhang), wangczlhs@sina.com (C. Wang).
Peer review under responsibility of King Saud University.

Production and hosting by Elsevier

https://doi.org/10.1016/j.arabjc.2023.104679
1878-5352 © 2023 The Author(s). Published by Elsevier B.V. on behalf of King Saud University.
This is an open access article under the CC BY-NC-ND license (http://creativecommons.org/licenses/by-nc-nd/4.0/).

anticancer activity, with IC_{50} of 0.56 μg/mL at 72 h. Besides, the anticancer mechanism study revealed that GBP-PBAE-Gal arrested the cell cycle in HepG2 cells, suggesting the potential of GBP-based carrier for intensive treatment. This research evidenced the feasibility and high availability of the GBP to use as a drug carrier, providing a novel candidate for drug delivery systems.

© 2023 The Author(s). Published by Elsevier B.V. on behalf of King Saud University. This is an open access article under the CC BY-NC-ND license (http://creativecommons.org/licenses/by-nc-nd/4.0/).

1. Introduction

Chemotherapy is the mainstay of cancer treatment to reduce pain and inhibits the further spread of cancer cells (Aapro et al., 2022, Blayney and Schwartzberg 2022). Unfortunately, chemotherapy drugs are usually small molecules that are poorly selective and strongly diffuse, leading to their treatment with various side effects (Guo et al., 2021). This is the direct cause to limit the dosage or use of chemotherapeutic drugs. In recent years, the advent of carrier materials has offered an opportunity for chemotherapeutic drugs to manage their distribution and selectivity in vivo and reduce their toxic side effects (Zhou et al., 2020, Ren et al., 2021, Zhang et al., 2022). The poly (cyclodextrin)-based nanocarriers have been reported that provide a solution for the poor stability and low therapeutic efficiency of chemotherapy drugs (Zhang et al., 2022). Chen et al designed a PEGylated dendritic polyurethane carrier for ultrasound-triggered localized drug delivery and enhancing the selectivity of doxorubicin to tumor cells (Chen and Liu 2022). Although the side effects of chemotherapy drugs have been improved to varying degrees via the delivery of developed drug carriers, the lacking of substantial physiological activity and low availability of the majority of drug carriers is still a problem (Chen et al., 2022, Lin et al., 2022). Therefore, developing a novel material with highly utilizability and pharmacological value to replace traditional material for drug carriers is a simple, versatile, and scalable method to improve the solubility, stability, and bioavailability of chemotherapy drugs (Mahdavi et al., 2022).

Natural bioactive ingredients derived from plants such as pectin, lycopene and polyprenol are ideal materials because they enjoy an overt medical effect and multiple bio-use properties, as well as a high level of safety and biocompatibility for human health, which can maximize the economic value of the carriers and achieve their high availability. Shehata et al. prepared pectin-coated nanostructured lipid carrier that achieved the targeted delivery of piperine to hepatocellular carcinoma and enhanced it anticancer effect in vivo (Shehata et al., 2022). Mennati et al. (2022) prepared a lycopene-loaded mPEG-PCL-DDAB carrier (methoxypoly (ethylene glycol)-poly(caprolactone)-dimethyl-dioctadecyl-ammonium bromide), which not only delivered anti-insulin-like growth factor 1 receptor-siRNA, but also induced the apoptosis and arrested cell cycle of MCF-7 cells. These studies have found that natural bioactive ingredients are no less effective than conventional carrier materials in terms of the delivery and therapeutic activity of drugs.

Polyprenol, a well-known class of natural lipid compounds, is composed of unsaturated isoprene units (from several up to more than 100 units), with antioxidant, antimicrobial, antivirus, and antitumor properties (Lichota et al., 2019, Gawrys et al., 2021). They are involved in cell response to environmental stress, glycosylation, and prenylation of proteins, intensifying the fusion and the permeability of model membranes (Gawrys et al., 2014, Grecka et al., 2016). Notably, polyprenol has been affirmed as a beneficial protectant for the liver (Yang et al., 2011) and statin-induced muscle weakness (Jansone et al., 2016), as an efficient drug carrier for delivering gene and antihypertensive drug (Gawrys et al., 2018, Rak et al., 2020). However, the main common plant sources for polyprenol on a commercial scale are *Abies sibirica L.* (Vanaga et al., 2020), *Picea abies L.*, *Pinus sibirica L.* and *Pinus sylvestris L.* (Muceniece et al., 2016, Pronin et al., 2021). Although polyprenol from *Ginkgo biloba L.* was the most abundant in the content (Boateng et al., 2021), rare studies have investigated it as a drug carrier until recently, mainly owing to the limitations associated with *Ginkgo biloba L.* polyprenol (GBP) extraction technology (Guo et al., 2021, Van Gelder et al., 2021). Fortunately, our research team has developed efficient and green methods to extract GBP with a purity of 99.8 % (Zhang et al., 2019, Zhang et al., 2020), and the GBP obtained by this technique was used to prepare liver protection capsules, micro- and nano-emulsions and liposome gels (Wang et al., 2015, Tao et al., 2016), which achieved good economic benefits of GBP. Nevertheless, there are no reported studies on the application of *Ginkgo biloba* polyprenol as a drug carrier for the delivery of anticancer drugs. Taking advantage of the lipid property and intensified membrane permeability of GBP, a GBP-based derivative was inspired and designed to use as a drug carrier for the delivery of chemotherapy drugs, with a view to achieve the efficient delivery of drugs and acting as an additional agent to enhance the therapy of cancer.

In this study, poly (β-amino ester) with pH-responsiveness was introduced into the structure of GBP as a linkage bridge to attach the targeted galactose fragments to synthesize a GBP-based derivative, as shown in Fig. 1. Further, the suitability and efficacy of GBP-based derivative as drug carrier was ascertained. Doxorubicin was chosen to investigate the drug loading capacity, stability, and in vitro drug release kinetics of GBP-based carrier. Meantime, the biocompatibility of GBP-based carrier was surveyed in terms of hemolysis rate and cytotoxicity. In addition, liver cancer HepG2 cells model was used to examine the anticancer activity of doxorubicin encapsulated into GBP-based carrier, and its anticancer mechanism was investigated via cell uptake, cell cycle, and western blotting.

2. Materials and methods

2.1. Materials

GBP with high purity (≥99.8 %) was obtained by the previous work of our research group (Zhang et al., 2020). Aminated GBP was got from Apptec Co., ltd. (WuXi, China). Triethylamine, dithiodiethanol, acryloyl chloride, anhydrous magnesium sulfate, 5-amino-1-pentanol (APA), dichloromethane (DCM) and galactosamine hydrochloride were all purchased from Shanghai Aladdin Biochemical Technology Co., ltd (Shanghai, China). 2,2-dithiodiethyl diacrylate (DSEA) was synthesized by our laboratory (details of the synthesis of DSEA were presented in the supplement of methods 1.1, its synthetic route was shown in Fig. S1, and its structure characterization of ^1H NMR was provided in Fig. S2). Fetal bovine serum was purchased from Thermo Fisher Scientific (Waltham, Massachusetts, USA). Human red blood cells (1 %), Human normal liver cell line (HL-7702) and HepG2 cells, triton-100 (X-100), trypsin-EDTA digestive fluid, dulbecco's modified eagle medium (DMEM), cell counting kit-8 (CCK-8), Hoechst33342, TUNEL detection kit, DAPI staining kit, total protein extraction kit, BCA protein content detection kit, SDS-page gel preparation kit, tris–glycine protein electrophoresis buffer, and western blotting detection kit were provided by Jiangsu Kaiji Biotechnology Co., ltd (Jiangsu, China).

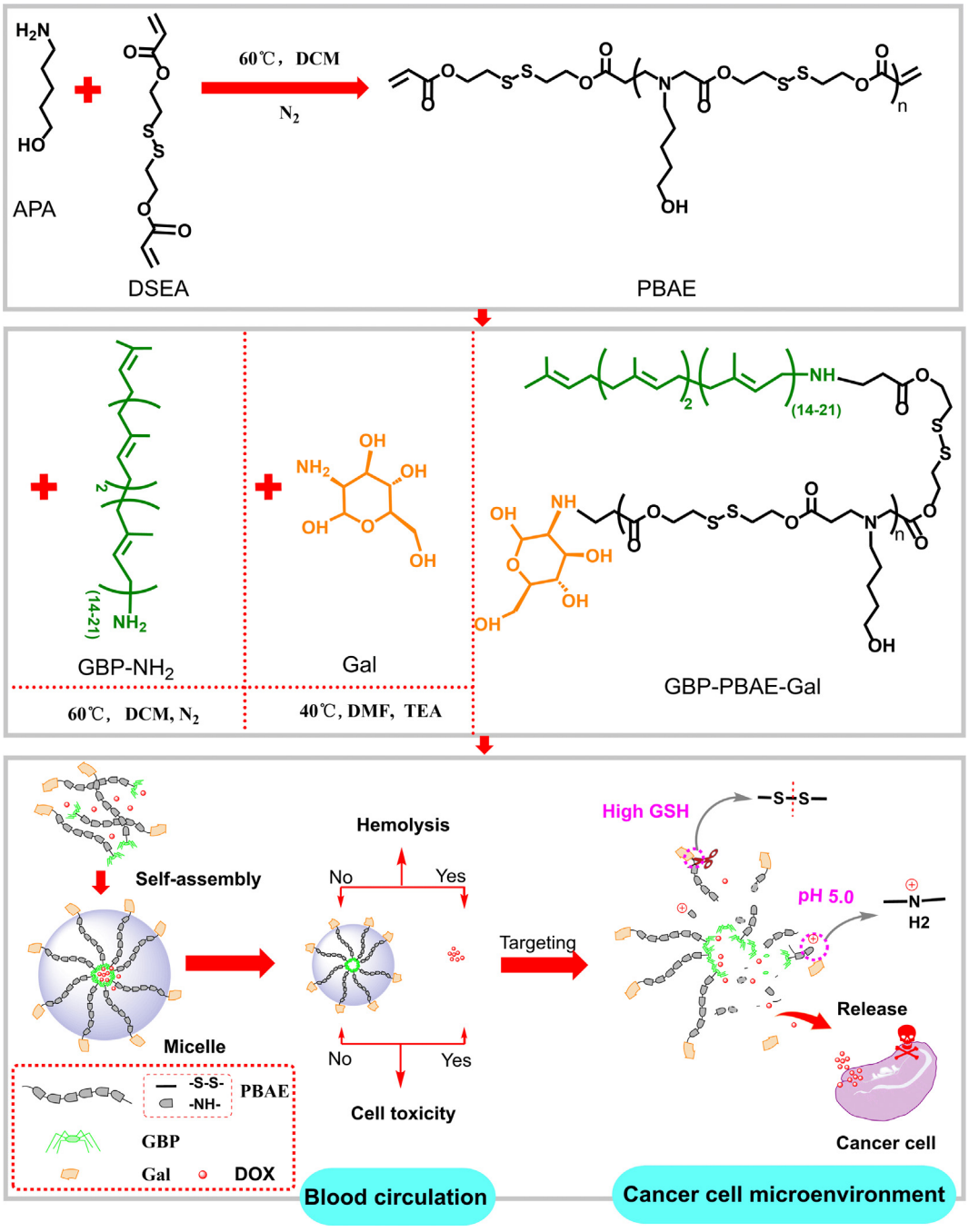

Fig. 1 Scheme for the design of GBP-based derivative as a drug carrier.

2.2. Synthesis of GBP-PBAE

First, the poly (β-amino esters) was synthesized by DSEA and 5-amino-1-pentanol by referring to the methods of Rui et al (Y. Rui 2022). The poly (β-amino esters) and aminated GBP were separately dissolved into 5 mL of anhydrous DMF according to the molar mass ratios of 2:3. Then, the mixture was reacted under the condition of 90 °C and nitrogen atmosphere for 72 h. Upon completion of the reaction, 50 mL of dichloromethane was poured into the mixture and then filtered and distilled in a vacuum. The obtained crude product was firstly dialyzed with the mixture of DCM and DMF (1:1, V:V) in a dialysis bag (1000 Da) for two days to remove the unreacted monomers, and followed dialyzed with water for 36 h. Finally, the GBP-PBAE was gained by freeze-drying.

2.3. Synthesis of GBP-PBAE-Gal

The 1-fold equivalent of galactosamine hydrochloride was reacted with the 1.2-folds equivalent of triethylamine in 10 mL of anhydrous DMF for 5 h to remove hydrochloride by referring to the research of Sharma et al (Sharma et al.,

2021). Then, the above synthesized GBP-PBAE and desalted D-galactosamine (Gal) were dissolved in DMF (molar ratio: 1:5) and reacted at 40 °C for 24 h. The GBP-PBAE-Gal was achieved by dialyzing with deionized water for 24 h and freeze-drying.

2.4. Micellization and DOX loading of GBP-PBAE-Gal

30 mg of GBP-PBAE-Gal was dissolved in 1 mL of anhydrous DMF, and then dropped into deionized water (29 mL). The mixture was stirred for 2 h at 25 °C and dialyzed for 24 h with a 1000 Da dialysis bag in deionized water to remove DMF. Then, the GBP-PBAE-Gal micelles were obtained after freeze-drying. The critical micelle concentration (CMC) of GBP-PBAE-Gal was measured using 1, 6-diphenyl-1,3,5-hextriene (DPH) as a UV molecular probe according to the reference (Calori et al., 2020).

The GBP-PBAE-Gal micelles (20 mg) and different masses of desalted DOX were redissolved in 5 mL of DMF and slowly dropped into 15 mL of deionized water. Then, the mixture was stirred for 12 h at 25 °C and dialyzed for 24 h with a 1000 Da dialysis bag in water (water change every 4 h). Meantime, the absorbance of water was detected at 480 nm to obtain the amount of free DOX based on the standard curve of DOX in water, and further to calculate the drug loading capacity (DLC) and encapsulation efficiency (EE) of GBP-PBAE-Gal micelles. The calculation equation is as follows:

$$DLC(\%) = \left[\left(M_{totalDOX} - M_{freeDOX}\right)\right] \times 100\% \quad (1)$$

$$EE(\%) = \left[\left(M_{totalDOX} - M_{freeDOX}\right)/M_{totalDOX}\right] \times 100\% \quad (2)$$

2.5. Characterization

The structure of DSEA, GBP-PBAE, and GBP-PBAE-Gal were characterized by FT-IR (Nicol iS50, USA) at 400–4000 cm^{-1} and ^1H NMR spectrometer (AVANCE III HD 600 MHz, Bruker, Karlsruhe, Germany). Using *N*-octanol–water as a dispersion system, the lipid water distribution coefficient of GBP-PBAE-Gal was detected by UV–vis spectrophotometry. The particle size and distribution of the blank micelle were measured by a Zeta sizer NanoZS90 particle size/zeta potential analyzer (Malvern Instruments, UK). The micellar morphology was observed with a transmission electron microscope (TEM, JEOL JEM 2100). The thermal stability of GBP-PBAE-Gal before and after loading DOX was determined using thermogravimetric analysis (TGA) (Netzsch TG209F1, Germany) under nitrogen flow with a heating rate of 10 °C/min in the range of 20–800 °C. The phase analysis of GBP-PBAE-Gal before and after loading DOX was determined by differential scanning calorimeter (DSC) (DSC 8000, UK) under nitrogen flow with a heating rate of 10 °C/min in the range of −60–40 °C.

2.6. Stability assay

To investigate the dilution stability, GBP-PBAE-Gal micelles were diluted from 1 to 640 times, and their size variation was detected by a Zeta sizer NanoZS90 particle size/zeta potential analyzer (Malvern Instruments, UK). To explore the long-term storage stability, GBP-PBAE-Gal micelles were reserved at room temperature for 30 days and the size variation was detected every 5 days. Then, 10 mL of GBP-PBAE-Gal micelles (1 mg/mL) was mixed with the same volume of DMEM containing 10 % (v/v) FBS and was subsequently kept at 37 °C, and their size variation at 2 h / times was measured to simulate their stability in blood.

2.7. pH and GSH stimuli-responsive disassembly

The pH and GSH co-triggered disassembly of GBP-PBAE-Gal micelles was investigated in different pH and GSH concentration buffer solutions via referring to the research of Park et al (Park et al., 2021). In brief, GBP-PBAE-Gal micelles were incubated in PBS at pH 5.0, 6.4, or 7.4 with 0 or 10 mM GSH for 0, 4, 8, and 12 h, respectively. The particle size distribution of the samples was subsequently monitored by a Nano laser particle size analyzer. Meanwhile, the potential change of GBP-PBAE-Gal micelles was researched.

2.8. DOX release

The phosphate buffer and reductive phosphate buffer (pH 5.0 + 10 mM GSH, pH 7.4 + 10 mM GSH, and pH 6.4 + 10 mM GSH) were simulated as a tumor microenvironment for forecasting the DOX release behavior from GBP-PBAE-Gal micelles in vivo. Briefly, 2 mL of DOX-loaded GBP-PBAE-Gal micelles (1 mg/mL) were loaded in a dialysis bag (MWCO 3.5 K Da) and dialyzed against 10 mL of the medium at 37 °C in a beaker with constant vibration. At pre-established times, 0.5 mL of release medium were withdrawn, replaced with fresh medium, and quantified by a UV/Vis spectrophotometer (λ = 480 nm). Then, DOX concentration in the release medium was measured by using a standard calibration curve of DOX prepared under the same conditions. The DOX cumulative release from micelles was calculated by following equation (3).

$$Cumulativerelease(\%) = \left(V_e \sum_{i}^{n-i} C_i + V_0 C_n\right)/m_{DOX} \quad (3)$$

Where V_e is the displacement volume of PBS, n is the number of times to replace PBS, C_i and C_n are the DOX concentration in the released medium at the i th and n th sampling, V_0 is the total volume of release medium, m_{DOX} is the weight of DOX contained in the nanoparticles.

To study the DOX release mechanism of GBP-PBAE-Gal micelles, four common empirical formulas (Zero order (Peppas 2014), First order (Li et al., 2022), Higuchi (Dehcheshmeh and Fathi 2019), and Korsmeyer-Peppas kinetics models (N.A. Peppas 1989) for evaluating drug release characteristics were applied to fit the release data. The four empirical formulas are as follows:

$$M_t/M_\infty = kt\,(\text{Zero order model}) \quad (4)$$

$$\ln\left[1 - (M_t/M_\infty)\right] = -kt\,(\text{First order model}) \quad (5)$$

$$M_t/M_\infty = kt^{0.5}(\text{Higuchi model}) \quad (6)$$

$$M_t/M_\infty = kt^n(\text{Korsmeyer} - \text{Peppas model}) \quad (7)$$

Where M_t/M_∞ is the fractional drug release percentage at time t, k is a kinetic constant correlated with the release properties, *and* n is the release index, which is used to characterize the release mechanism of drugs. ($n < 0.43$, co-control by diffusion-erosion; $n = 0.43$, Fickian diffusion; $0.43 < n < 1$, multiple mechanisms effect in tandem: skeleton dissolution and drug diffusion, n greater than 1, Zero-order release, which is controlled by the structural change dynamics of polymer.).

2.9. In vitro biocompatibility

The biocompatibility of GBP-PBAE-Gal micelles was surveyed in terms of hemolysis test and cytotoxicity to human normal liver cell line (HL-7702). Briefly, 2 mL of GBP-PBAE-Gal micelles with a series of concentrations of 0.0025–2 mg/mL were incubated with an equivalent volume of human red blood cell (1 %) suspension under the oscillations for 2 h at 37 °C. The triton-100 (X-100) was taken as positive control and normal saline was taken as the negative control. Then, the absorbance at 540 nm of the supernatant of samples was measured respectively and their hemolysis ratio was calculated according to the following formula (8).

$$Hemolysisratio(\%) = \left[(OD_t - OD_n)/(OD_t - OD_p)\right] \times 100\% \quad (8)$$

where OD_t, OD_n, and OD_p are the absorbance of the treatment groups, negative (normal saline) and positive (X-100) controls, respectively.

The human normal liver cells HL-7702 were selected to evaluate the cytocompatibility of GBP-PBAE-Gal micelles using the CCK-8 method. In brief, the HL-7702 cells were co-cultured with the desired concentration of GBP-PBAE-Gal micelles with a density of 4.0×10^4 cells /well under 5 % of CO_2 humidified atmosphere at 37 °C for 24 h. Then, the absorbance of each well was measured at 450 nm by a microplate reader (EL-x800, BioTek Instruments, USA) and the inhibition rate of HL-7702 was calculated according to Equation (9).

$$Inhibitionrate(\%) = \left[(OD_{control} - OD_{sample})/(OD_{control} - OD_{blank})\right] \times 100\% \quad (9)$$

where OD_{sample} is the absorbance of the cells treated with drugs, $OD_{control}$ is the absorbance of the cells without drugs, *and* OD_{blank} is the absorbance of the blank medium without cells and drugs.

2.10. Anticancer efficacy

HepG2 cells were used to evaluate the anticancer activity of GBP-PBAE-Gal by the CCK-8 method. In detail, 100 μL of HepG2 cells suspension were cultured onto a 96-well plate with a density of 4.0×10^4 cells /well under a 5 % CO_2 atmosphere at 37 °C for 24 h. Then, 100 μL of the corresponding medium containing the desired concentration of samples was added at 0, 24, and 48 h, and incubation continued for 72, 48, and 24 h, respectively. The fresh medium without any drug was utilized as the negative control group. After that, the HepG2 cells were stained with CCK-8 and their OD values were determined at λ = 450 nm by a microplate reader (EL-x800, BioTek Instruments, USA). The inhibition rate of according to Equation (9).

2.11. Anticancer mechanism

The anticancer mechanism of DOX-loaded GBP-PBAE-Gal micelles was discussed by the studies of cell uptake, targeting performance analysis, cell cycle, cell apoptosis, and western blotting on HepG2 cells. The specific experimental methods are presented in methods 1.2–1.6 of the supporting material.

2.12. Statistical analysis

Data are presented as the mean ± standard deviation (error bars) from at least three individual measurements. The student's *t*-test was used to analyze the difference between the two samples. Experimental values were considered to be significantly different at the P-value < 0.05.

3. Results and discussion

3.1. Characterization of GBP-PBAE-Gal

The GBP-PBAE-Gal was first synthesized by Michael additive reaction of poly (β-amino esters) (PBAE) containing disulfide bonds with amino-GBP and galactose, its structure characterization was shown in Fig. 2. In the ^{1}H NMR of PBAE (Fig. 2A), the signals at 1.3–1.6 ppm were assigned to –CH_2-CH_2-CH_2-, the signals of 2.4 ppm and 2.9 ppm belonged to the protons that abutted to carbonyl and nitrogen atoms, respectively, and the symbolic signals of –CH = CH– at the end of PBAE were found at 5.8 ppm and 6.2–6.5 ppm, respectively, indicating that the PBAE was synthesized (Chaudhuri et al., 2021). The degree of polymerization (n) of PBAE was calculated to be 10 based on the peak area ratio of double bonds to the repeating group, and the molecular weight of PBAE was approximately 3200 in combination with its GPC measurement result (Fig. 2B). In the ^{1}H NMR analysis of GBP-PBAE (Fig. 2C), the characteristic peaks at 5.4 ppm (-C═C─C═C─H), 5.1 ppm ($(CH_3)_2$C = C─H), 4.1 ppm (C–C═C-CH_2-), 2.2–2.0 ppm (4H, -C = CCH_2CH_2C = C-), 2.0–1.9 ppm (CH_3-C–C═C-), 1.8–1.5 ppm (CH_3-C═C-) were ascribed to the proton signals of GBP-NH_2 (Fig. S3). The characteristic proton signals of the PBAE block at 1.3–1.6 ppm, 2.5 ppm, and 2.7 ppm appeared. In addition, looking at the FT-IR spectrum of GBP-PBAE in Fig. 2D, the typical absorptions appeared at 3367 cm^{-1} and 1734 cm^{-1}, which are ascribable to the branched-chain hydroxyl groups and C═O groups of PBAE bands, and the medium-strong peak at 1172 cm^{-1} caused by the bending vibration of C─N in the main chains of PBAE. These results confirmed the successful preparation of GBP-PBAE. In ^{1}H NMR of GBP-PBAE-Gal, a wide peak signal of the sugar ring of galactose emerged at 3.2–3.5 ppm. Meanwhile, it was obvious that the alkenyl signal of PBAE at 5.8–6.5 ppm disappeared, indicating the successful sealed-modification with galactoses of GBP-PBAE. Combining the FT-IR spectrum of GBP-PBAE-Gal, it is obvious that the wide peak between 3100 cm^{-1} and 3500 cm^{-1} was generated after the sealed modification with galactoses, which

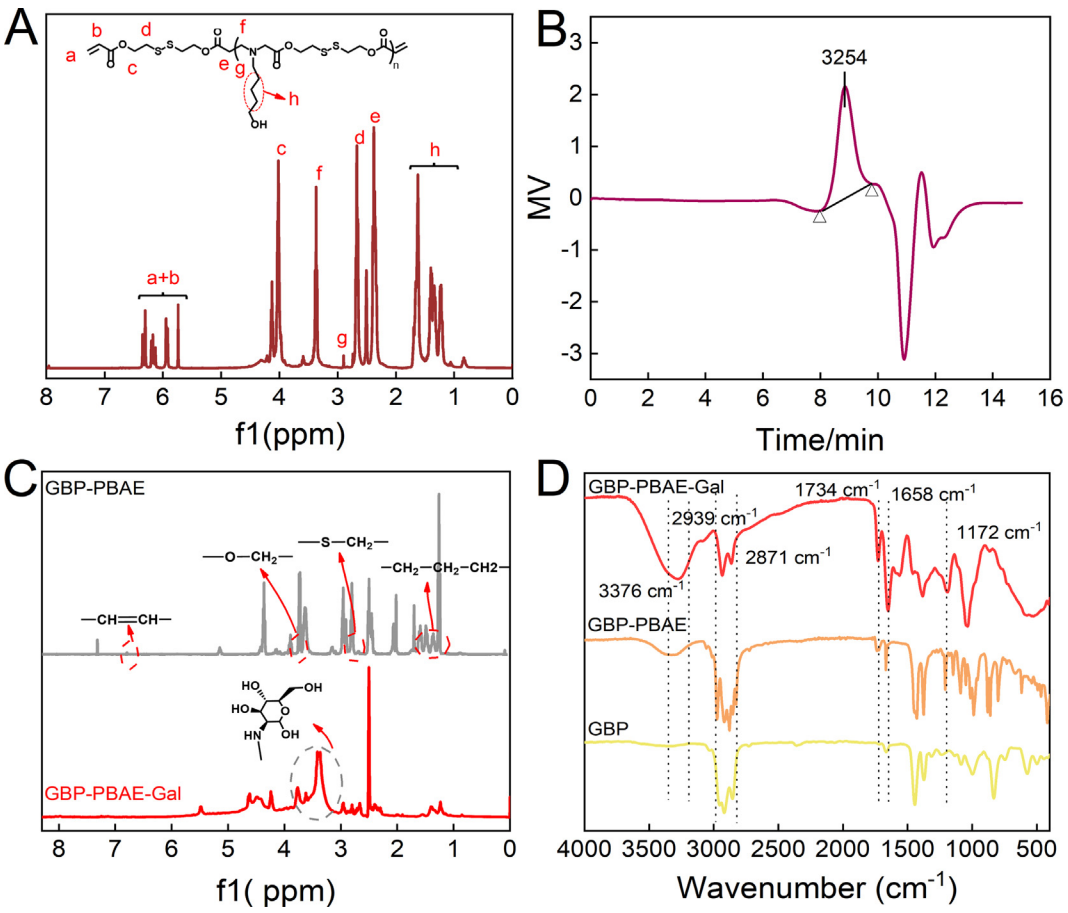

Fig. 2 The ^{1}H NMR spectrum (A) and gel permeation chromatography spectra of poly (β-amino esters) (B) and the ^{1}H NMR spectrum (C) and FI-IR (D) of GBP-PBAE-Gal.

came from the hydroxyl groups of galactoses. Meanwhile, the new absorption peak appeared at 1658 cm^{-1}, which resulted from the –NH- of the galactoses. The results further demonstrated the successful synthesis of GBP-PBAE-Gal. Besides, the lipid water distribution coefficient of GBP-PBAE-Gal was determined to be 2.46 in *N*-octanol–water (Table S1).

3.2. Self-assembly and DOX loading of GBP-PBAE-Gal

The amphiphilic character of GBP-PBAE-Gal allowed it to self-assemble into micelles in deionized water. It was hypothesized that the hydrophobic core of GBP-PBAE-Gal micelles was constituted by hydrophobic domains GBP-PBAE, while the hydrophilic galactose formed its shell. The self-assembling capability of GBP-PBAE-Gal micelles was evaluated by measuring its critical micelle concentration (CMC), the result was depicted in Fig. 3A. The lower the CMC value, the stronger the self-assembly capacity of the micelles, which means better stability of the micelles (Qiu et al., 2022). From the crossover points of the curve between the logarithm of micellar concentration and absorbance, the CMC of GBP-PBAE-Gal was 7.64 μg/mL. Next, DOX was employed as a model drug to investigate the loaded capacity and encapsulation property of GBP-PBAE-Gal micelles. The different concentration of DOX was loaded by the hydrophobic interaction of GBP-PBAE-Gal micelles. In Fig. 3B, the DOX-loaded capacity of GBP-PBAE-Gal micelles increased with the growing concentration of DOX. This may be because the hydrophobic core of GBP-PBAE-Gal micelle has a strong hydrophobic effect on DOX, which can aggregate more DOX (Sahkulubey Kahveci et al., 2022). However, the encapsulation property decreased with the increase of DOX. This result explained that the limited space of the hydrophobic core of GBP-PBAE-Gal micelles did not guarantee the complete package of excess DOX. When the ratio of 1:0.3 (micelle and DOX), the GBP-PBAE-Gal micelles were equipped with a high encapsulation rate (93.10 ± 2.51 %) and a suitable drug loading (28.62 ± 1.49 %) for DOX. Therefore, for the comprehensive consideration of encapsulation rate and drug loading, the appropriate proportion is 1:0.3 for GBP-PBAE-Gal micelles and DOX, and the resulting DOX-loaded GBP-PBAE-Gal micelles (GBP-PBAE-Gal@DOX) was used as the object of the subsequent experiment.

Further, to verify DOX was loaded into GBP-PBAE-Gal micelles, the ultraviolet absorption spectrum and transmission electron microscopy (TEM) of GBP-PBAE-Gal@DOX micelles were investigated, as shown in Fig. 3C and D. TEM observation revealed the morphology of both GBP-PBAE-Gal blank micelles and GBP-PBAE-Gal@DOX micelles are spherical with uniform size distributions, and their mean diameter value was 109 ± 2.54 nm. In addition, it is obvious from the TEM of GBP-PBAE-Gal@DOX micelles that the DOX

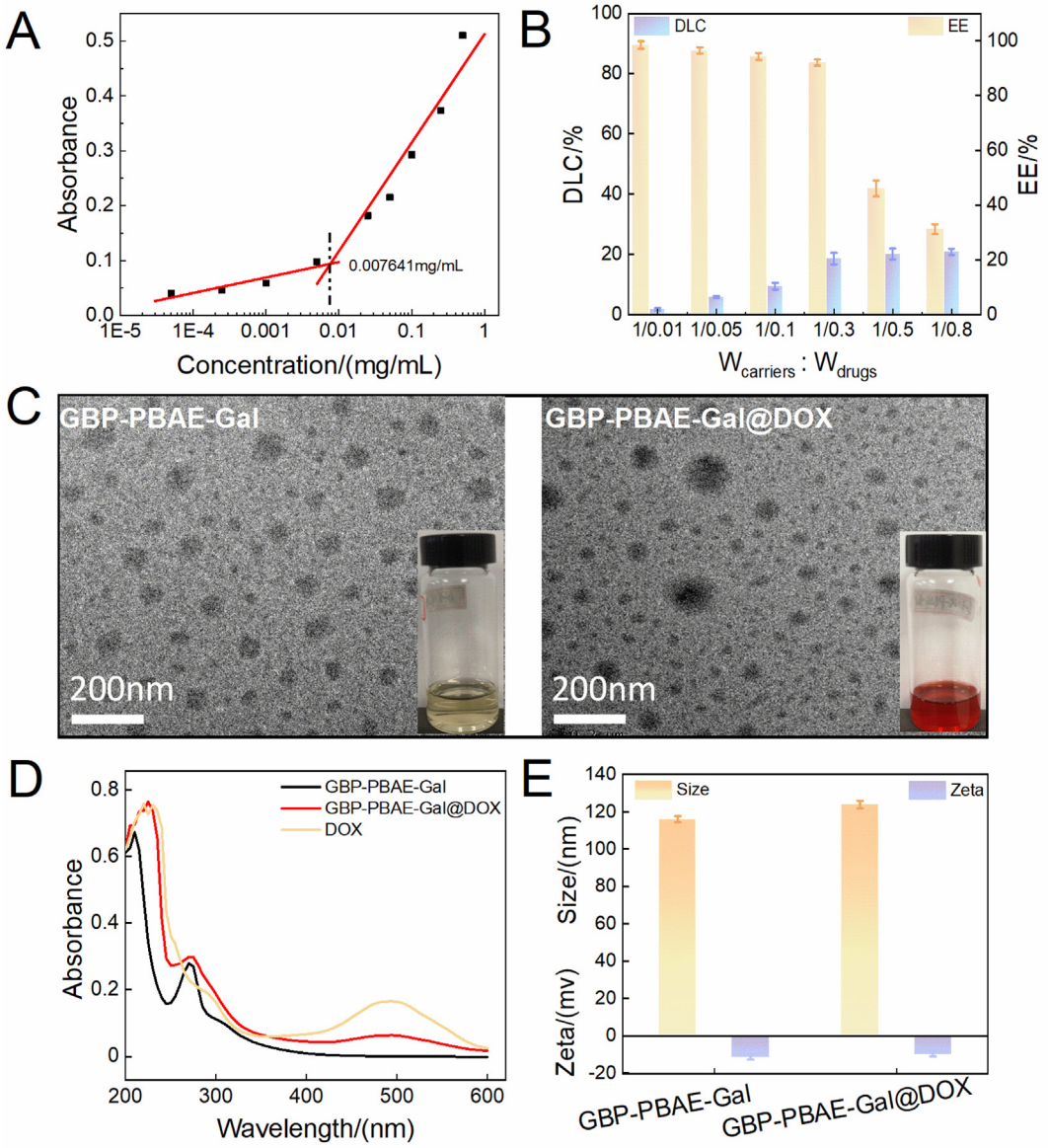

Fig. 3 The critical micelle concentration of GBP-PBAE-Gal micelles (A) and its loading capacity for DOX (B) (mean ± SD, n = 3), the transmission electron microscopy (C) and ultraviolet spectrogram (D) of GBP-PBAE-Gal micelles before and after loading DOX, as well as the partical size and zeta potential of GBP-PBAE-Gal micelles before and after loading DOX (E) (mean ± SD, n = 3).

were wrapped into GBP-PBAE-Gal micelles, and formed a shell-core structure. This result was also confirmed by the UV spectra of GBP-PBAE-Gal@DOX micelles in Fig. 3D. Both free DOX and GBP-PBAE-Gal@DOX micelles presented the maximum absorption at 485 nm, indicating the existence of DOX in GBP-PBAE-Gal@DOX micelles. Moreover, the particle size of GBP-PBAE-Gal@DOX micelles was tested by a Nano laser particle size analyzer. The analyzed results in Fig. 3E presented a unimodal distribution for GBP-PBAE-Gal micelles and GBP-PBAE-Gal@DOX micelles. The GBP-PBAE-Gal@DOX micelles possessed an average diameter of 116 ± 3.71 nm with PDI of 0.20. The zeta potential of the micelles was approximately −9.50 ± 1.53 mV. Compared to the size of GBP-PBAE-Gal blank micelles (110 ± 2.03 nm, with PDI of 0.13), the particle size of GBP-PBAE-Gal@DOX micelles was slightly larger, which is probably related to the occupied space of polymer micelle by DOX (Surya et al., 2020). Notably, the relatively small nanoparticle size of GBP-PBAE-Gal@DOX micelles will promote its enrichment in cancerous areas via the enhanced permeability and retention (EPR) effect.

3.3. Stability analysis

The existential state of drugs in the drug carrier has a significant impact on their stability and bioavailability. In general, the amorphous state of drugs was provided with a higher solubility and dissolution rate than the crystalline form and exhibits higher bioavailability (Edueng et al., 2022). The differential thermogravimetric analysis (DTG-TG) and differential scanning calorimetry (DSC) of GBP-PBAE-Gal@DOX micelles were shown in Fig. 4 A-C. The DTG-TG curves

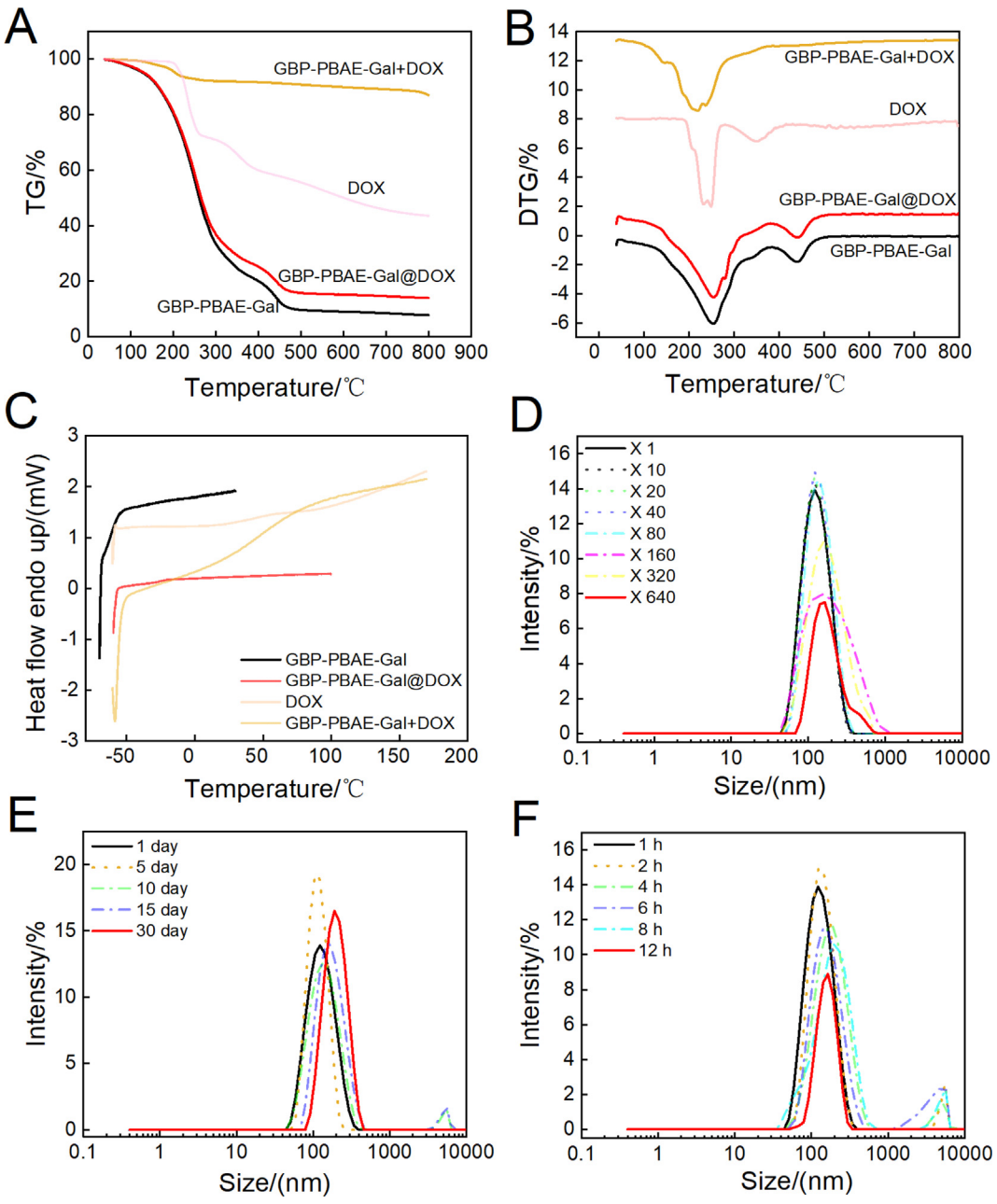

Fig. 4 The differential thermogravimetric analysis (A and B) and differential scanning calorimetry (C) of GBP-PBAE-Gal@DOX micelles, and the stability of GBP-PBAE-Gal@DOX micelles at the dilution (D), storage at room temperature (E) and in the presence of serum (F).

(Fig. 4A and B) of GBP-PBAE-Gal micelles and GBP-PBAE-Gal@DOX micelles displayed significant weight losses at above 100 °C, which was the result of GBP-PBAE-Gal micelles degradation. The first weight loss of the physical mixture GBP-PBAE-Gal + DOX at 215 °C was similar to that of free DOX, indicating that the DOX in the physical mixture GBP-PBAE-Gal + DOX was still present in a separate phase of the crystalline state. In contrast, no weight loss behavior of DOX was observed in the weight loss curve of the GBP-PBAE-Gal@DOX micelles, testifying that the DOX had been encapsulated into the GBP-PBAE-Gal@DOX micelles to form a holistic phase with them, resulting in the different DTG-TG curve of GBP-PBAE-Gal@DOX micelles and physical mixture GBP-PBAE-Gal + DOX. Based on the DTG-TG analysis results of the above samples, their DSC was further analyzed. As shown in Fig. 4C, free DOX was mainly crystalline state because an absorption peak existed at 50–75 °C. GBP-PBA-Gal micelles and GBP-PBAE-Gal@DOX micelles were amorphous without melting point, meaning that DOX was stored in the GBP-PBAE-Gal micelles in an amorphous state after being encapsulated, which was favorable to improve its solubility and bioavailability (Arafa et al., 2022). The melting peak of DOX still existed in the physical mixture GBP-PBAE-Gal + DOX, illustrating that DOX was present in crys-

talline form after physical mixing. Therefore, both DSC and DTG-TG results revealed that DOX had been encapsulated into GBP-PBAE-Gal micelles.

Further, the stability of dilution, storage as well as in the presence of serum for GBP-PBAE-Gal@DOX micelles were assessed by monitoring the changes in size, as shown in Fig. 4-D-F. The micellar size had not increased appreciably after dilution of 640 times, indicating that the micelles maintained their structural integrity during the dilution process, and allowed for long circulation in the blood. The micellar PDI fluctuated in the range of 0.1–0.2 after dilution (Fig. S4A), indicating the minor disturbance of dilution to micelle structure. This result was attributed to the hydrophobic components (GBP and PBAE blocks) forming the micellar core, whose hydrophobic interactions allow GBP-PBAE-Gal@DOX micelles to maintain a relatively even particle distribution in the extreme dilution (Zhang et al., 2022). The storage stability study (Fig. 4E and Fig. S4B) displayed the small fluctuation of particle size and PDI for GBP-PBAE-Gal@DOX micelles after 30 days of storage at room temperature, which mapped its admirable storage stability without special stimulation. Meanwhile, the stability in the presence of serum discovered that the size variation was inconspicuous for GBP-PBAE-Gal@DOX micelles within 12 h, manifesting they could retain their structural integrity during blood circulation, which is important for the micelle to avoid premature leakage of the drug in vivo.

3.4. Micellar destabilization triggered by pH and GSH

To investigate the pH- and GSH-responsiveness of GBP-PBAE-Gal@DOX micelles, the evolutions of particle size and potential were detected over 12 h as they were exposed to a variety of simulated environments. As depicted in Fig. 5A and B, there was no evident change in size and potential for GBP-PBAE-Gal@DOX micelles at pH 7.4. In contrast, a gradual size increase and change of potential for GBP-PBAE-Gal@DOX micelles were observed after the incubation at acid pH and acid pH containing 10 mM GSH. After the incubation in PBS at pH 5.0, the particle size of GBP-PBAE-Gal@DOX micelles produced a bimodal distribution and a more pronounced change in potential. The potential of GBP-PBAE-Gal@DOX micelles increased from −10.21 to 3.36 mV, which is the result of the protonation of the tertiary

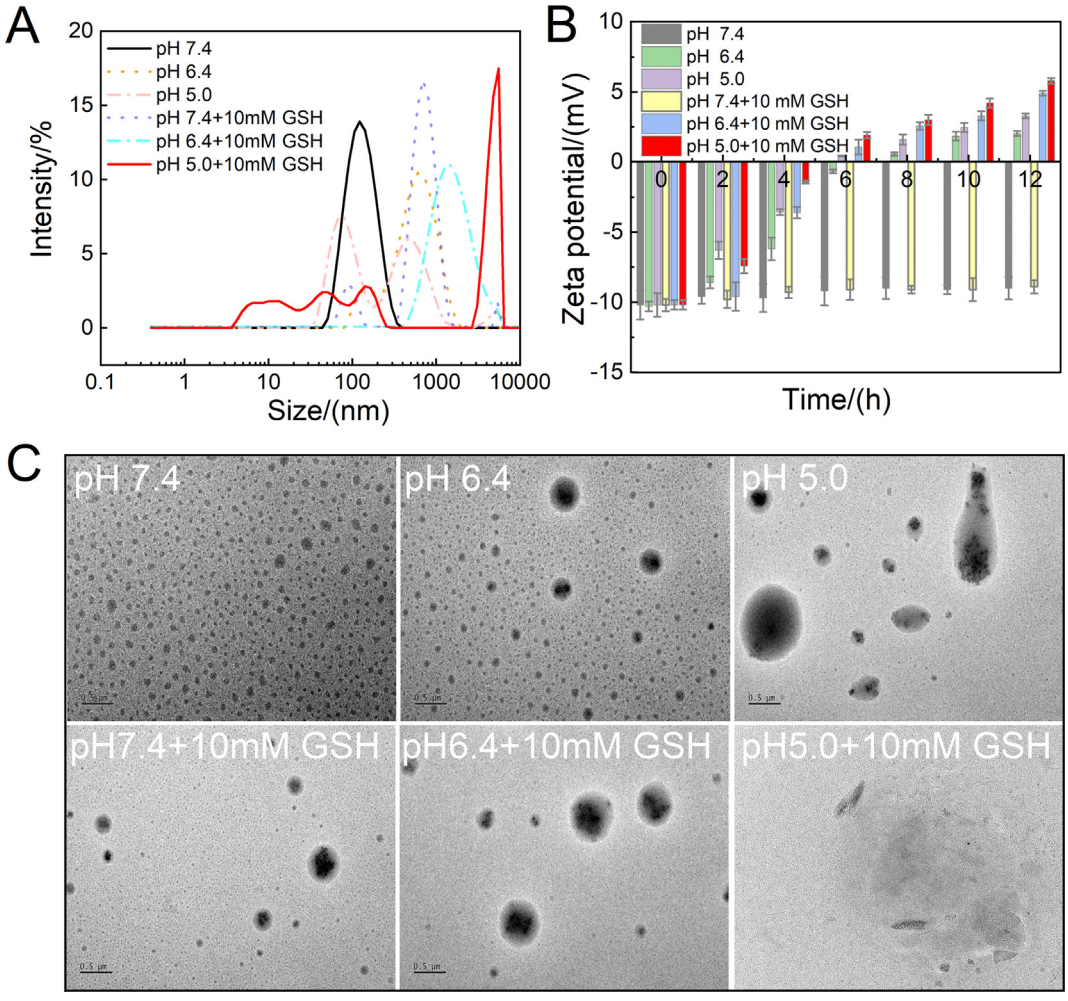

Fig. 5 The evolutions of particle size (A) and zeta potential (B) of GBP-PBAE-Gal@DOX micelles at acid pH and acid pH containing 10 mM GSH (mean ± SD, n = 3), and the photographs of GBP-PBAE-Gal@DOX micelles in different medium observed by transmission electron microscope (TEM) (C) (Scale bars: 500 nm).

amino group in PBAE fragments under acidic conditions (Wang et al., 2022). After incubating in pH 7.4 + 10 mM GSH, the particle size still kept a single peak distribution but took on greater than 600 nm with a PDI of 0.7, which is due to the breakage of S—S bonds in the presence of GSH, resulting in several small fragments interacting to form large particles (Zhan et al., 2022). Notably, the particle size of GBP-PBAE-Gal@DOX micelles occurred trimodal distribution, and the potential raised to 5.83 mV at pH 5.0 + 10 mM GSH, verifying that it was highly sensitive to pH and GSH, which would be facilitated the controlled release of drugs. At the same time, the GBP-PBAE-Gal@DOX micelles in different pH and different pH with 10 mM GSH media were placed on a copper grid to observe their structural changes, as shown in Fig. 5C. It is clear that the structure of GBP-PBAE-Gal@DOX micelles maintained integrity without change in pH 7.4, but showed a phenomenon of increasing size and varying degrees of swelling as well as deformation after incubation in the medium of acidic pH or acidic pH + 10 mM GSH. Notably, the structure of GBP-PBAE-Gal@DOX became collapsed under the dual effect of pH 5.0 and 10 mM GSH, which echoed the high release rate of DOX in the release profile. The results made clear that GBP-PBAE-Gal@DOX micelles possess quick responsiveness in the cancer environment, allowing for the effective release of DOX.

3.5. DOX release and mechanism

A stimuli-responsive drug delivery system is expected to quickly release its payload when reached the targeted tissues

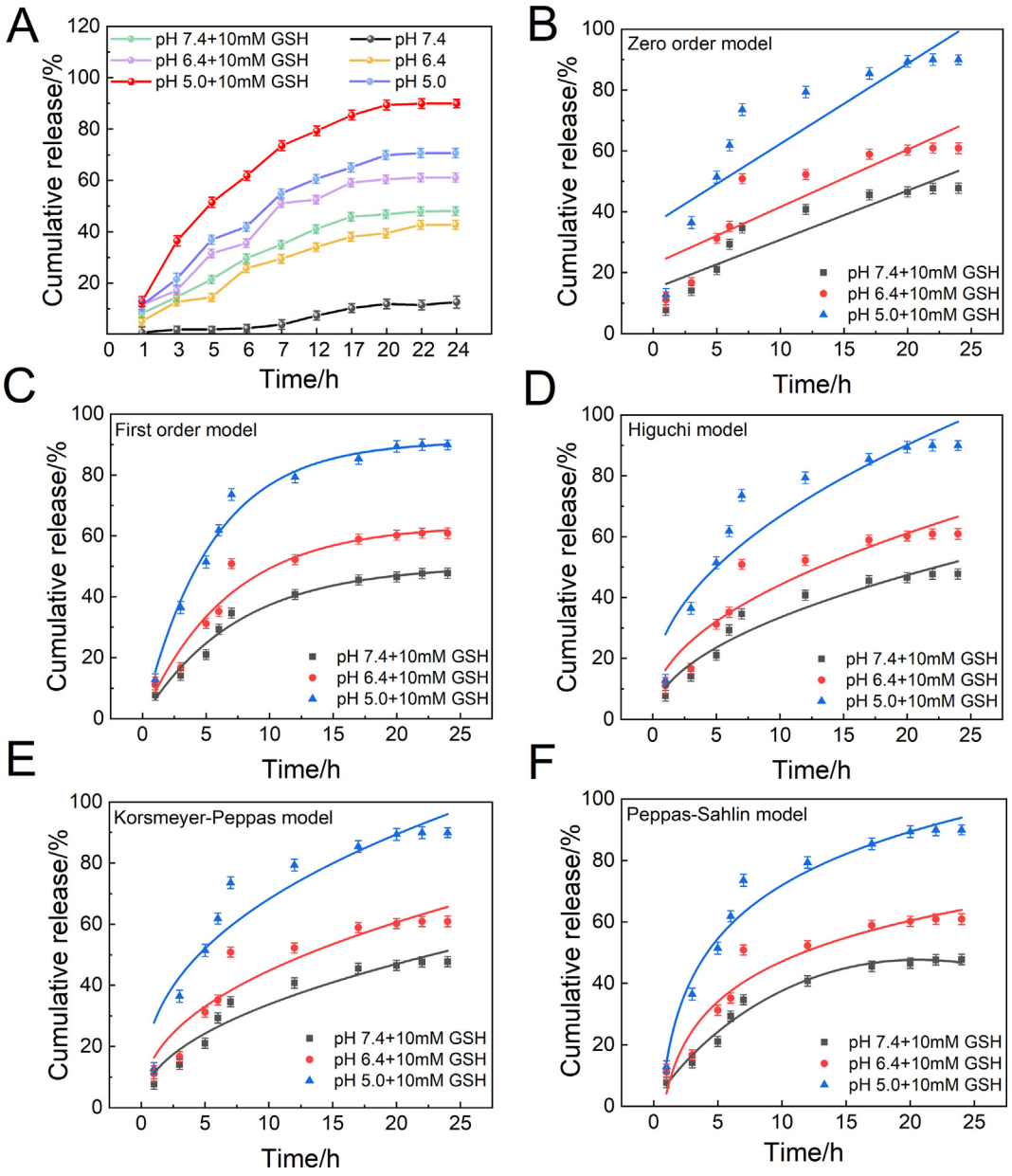

Fig. 6 In vitro release profile of DOX from GBP-PBAE-Gal@DOX micelles (A) (mean ± SD, n = 3) and its release fitting curves: Zero order model (B), First order model (C), Higuchi model (D), Korsmeyer-Peppas model (E), Peppas-Sahlin model (F) under the pH/GSH dual medium.

or cells (van der Vlies et al., 2022). Release experiments of GBP-PBAE-Gal@DOX micelles were performed in media mimicking the physiological conditions and the intracellular environment of the tumor. The controlled release profile was recorded in Fig. 6 A. There was a minimal release of DOX after the incubation under simulated normal physiological conditions (pH 7.4) for 24 h, and the cumulative release of DOX did not exceed 10 %. This result reflected the fact that GBP-PBAE-Gal@DOX micelles are stable in normal physiologic conditions and can avoid drug leakage during drug delivery. However, DOX was released to varying degrees after incubation in the simulated intracellular environment of cancer cells. The cumulative release of DOX was achieved at 70.54 %, 42.41 %, and 47.80 % in a single release medium at pH 5.0, 6.4, and 10 mM GSH, respectively. Comparing to a single stimulus-responsive medium, the release of DOX from GBP-PBAE-Gal@DOX micelles was significantly faster under a mix of acidic and reducing media. 90.30 % of DOX were released cumulatively in the medium of pH 5.0 + 10 mM GSH, which suggested that the dual response of pH and GSH for GBP-PBAE-Gal@DOX micelles endowed them with better selective drug release performance. There are two main reasons for this result: on the one hand, the micelle structure was disrupted by the reductive breakage of the -S—S- bond in the presence of a high concentration of GSH, and on the other hand, the PBAE blocks were completely exposed to the acidic cellular environment due to the breakage of -S—S- bond, which accelerated its protonation process and prompted a faster release of DOX (Liu et al., 2022). Furthermore, the cumulative release of DOX (60.92 %) was slightly lower at pH 6.4 + 10 mM GSH than that of pH 5.0 medium, which may be due to the GSH-response being predominantly dominant at pH 6.4 + 10 mM GSH compared with the gentle protonation of PBAE blocks under weakly acidic conditions, resulting that a part of DOX was tightly wrapped by hydrophobic BP-PBAE core and cannot be released effectively (Y. Rui 2022).

The release mechanism of GBP-PBAE-Gal@DOX micelles in six different media was investigated using Zero order, First order, Higuchi, and Korsmeyer-Peppas kinetics models. Fig. 6-B-E and Fig. S5A-D presented the main fitting results of four models under pH-response and pH/GSH dual response. In terms of the correlation coefficients (R^2) of four models in Table S2, a certain degree of differences emerged in the model fitting degree to the different release processes. The DOX release from GBP-PBAE-Gal@DOX micelles at pH 7.4 conformed to the Zero-order model with the greatest R^2 of 0.99. At acid pH (5.0 or 6.4) and pH (5.0, 6.4, or 7.4) + 10 mM GSH, the DOX release from GBP-PBAE-Gal@DOX micelles had a better fitting result in First-order release model and Korsmeyer-Peppas model (R^2 greater than 0.94). According to the theory of First-order release model, the DOX loaded into GBP-PBAE-Gal micelles was released via the mechanism of dissolution and diffusion at acid pH and acid pH containing 10 mM GSH. Meanwhile, the *n*-values were mainly between 0.43 and 1 according to the Korsmeyer-Peppas model, further indicating that the DOX release from GBP-PBAE-Gal@DOX micelles was mainly achieved by the combination of Fickian diffusion and dissolution. The DOX release process of GBP-PBAE-Gal@DOX micelles was illustrated in Fig. S6. In the environment containing exorbitant GSH, the -S—S- bonds of GBP-PBAE-Gal@DOX micelles were broken and certain pore channels are created, achieving the first release pathway of DOX. Following, the hydrolysis of the ester bond and the protonation of PBAE fragments in the micelle structure of GBP-PBAE-Gal@DOX under the acidic environment made it turn to be water-soluble and accomplished the second release pathway of DOX. Therefore, the united induction routes of pH and reduction can greatly enhance the efficient release of DOX.

To further understand the proportion of relaxation (dissolution) mechanism (R) and diffusion mechanism (F) in the DOX release process, the Peppas-Sahlin model was used to analyze the release data of GBP-PBAE-Gal@DOX micelles, and the change of R/F value over time was shown in Fig. S5F. When R/F = 1, the release mechanism contained both dissolution and diffusion equally. If R/F greater than 1, the relaxation (dissolution) dominates, while for R/F < 1, diffusion dominates (Chiaregato and Faez 2021). The R/F value of GBP-PBAE-Gal@DOX micelles was < 1 at pH 7.4, the release of GBP-PBAE-Gal@DOX micelles was mainly con-

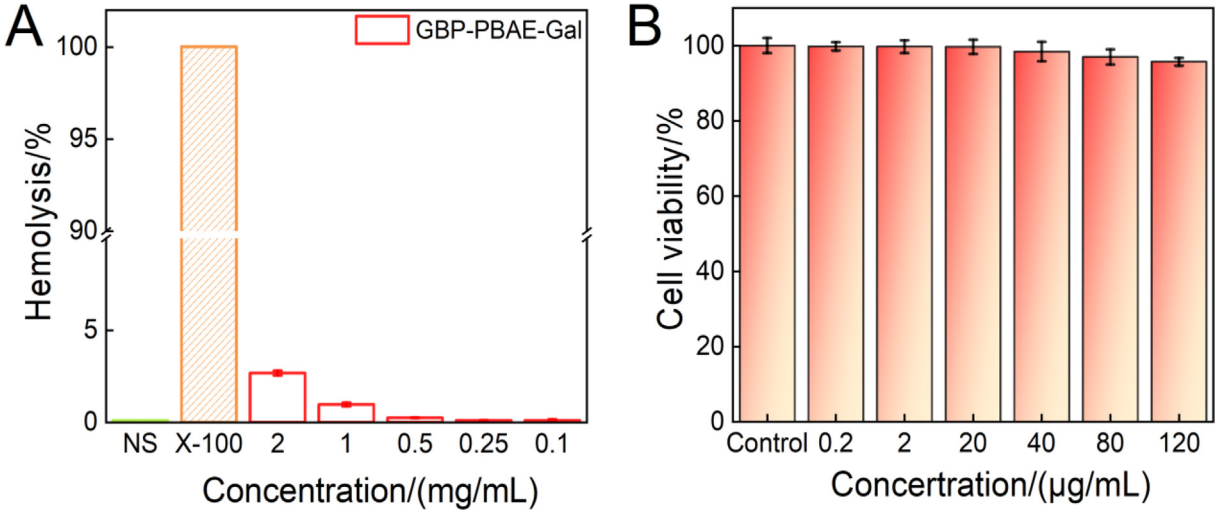

Fig. 7 Hemolysis assays of GBP-PBAE-Gal@DOX micelles at different concentrations (A) (mean ± SD, n = 3), and in vitro cytotoxicity (B) of GBP-PBAE-Gal@DOX micelles and free DOX against normal liver cells HL-7702 at 24 h (mean ± SD, n = 3).

trolled by the Fickian diffusion. Then, the R/F value of GBP-PBAE-Gal@DOX micelles increased with time at acid pH and acid pH + 10 mM GSH, particularly in co-media of acid pH + 10 mM GSH. Their R/F value was greater than 1, inferring that the DOX release from GBP-PBAE-Gal@DOX micelles was dominated by dissolution mechanisms, which was derived from their responsive structure to environmental stimulation that can disintegrate via the breaking of disulfide bonds and the protonation of PBAE segments.

3.6. In vitro biocompatibility

The hemolysis test is an important index to evaluate the biocompatibility of drugs, and the more compatible drugs generally have a hemolysis ratio of < 5 % (Shukla et al., 2022). The result of GBP-PBAE-Gal micelles in vitro hemolysis test of human red blood cells (RBC) was shown in Fig. 7A. The hemolysis ratio of GBP-PBAE-Gal micelles was far < 5 % in the range of 0.1–2 mg/mL, indicating that GBP-PBAE-Gal micelles were highly compatible with human RBC and would not cause strong hemolytic effect. Meantime, the appearance of human RBC treated with GBP-PBAE-Gal micelles was shown in Fig. S7A. The precipitated RBC were observed in the GBP-PBAE-Gal group after centrifugation, consistent with the state of normal saline (negative control group). Conversely, there were a bright red solution and no sediment of RBC in X-100 (positive control group), rendering an indication of a hemolytic effect. Morphological changes of RBC were further observed by optical microscopy, as shown in Fig. S7B. The morphology of RBC treated by GBP-PBAE-Gal micelles was intact and round, whereas the morphology of RBC treated with X-100 showed obvious deformation and rupture, suggesting that GBP-PBAE-Gal micelles are safe for human RBC. GBP-PBAE-Gal micelles were co-incubated with human normal liver cells HL-7702 for 24 h at different concentrations to evaluate it cytocompatibility, as shown in Fig. 7B. The results show that the cell viability is 95 % after 24 h incubation for the concentration of 120 μg/mL, suggesting the high

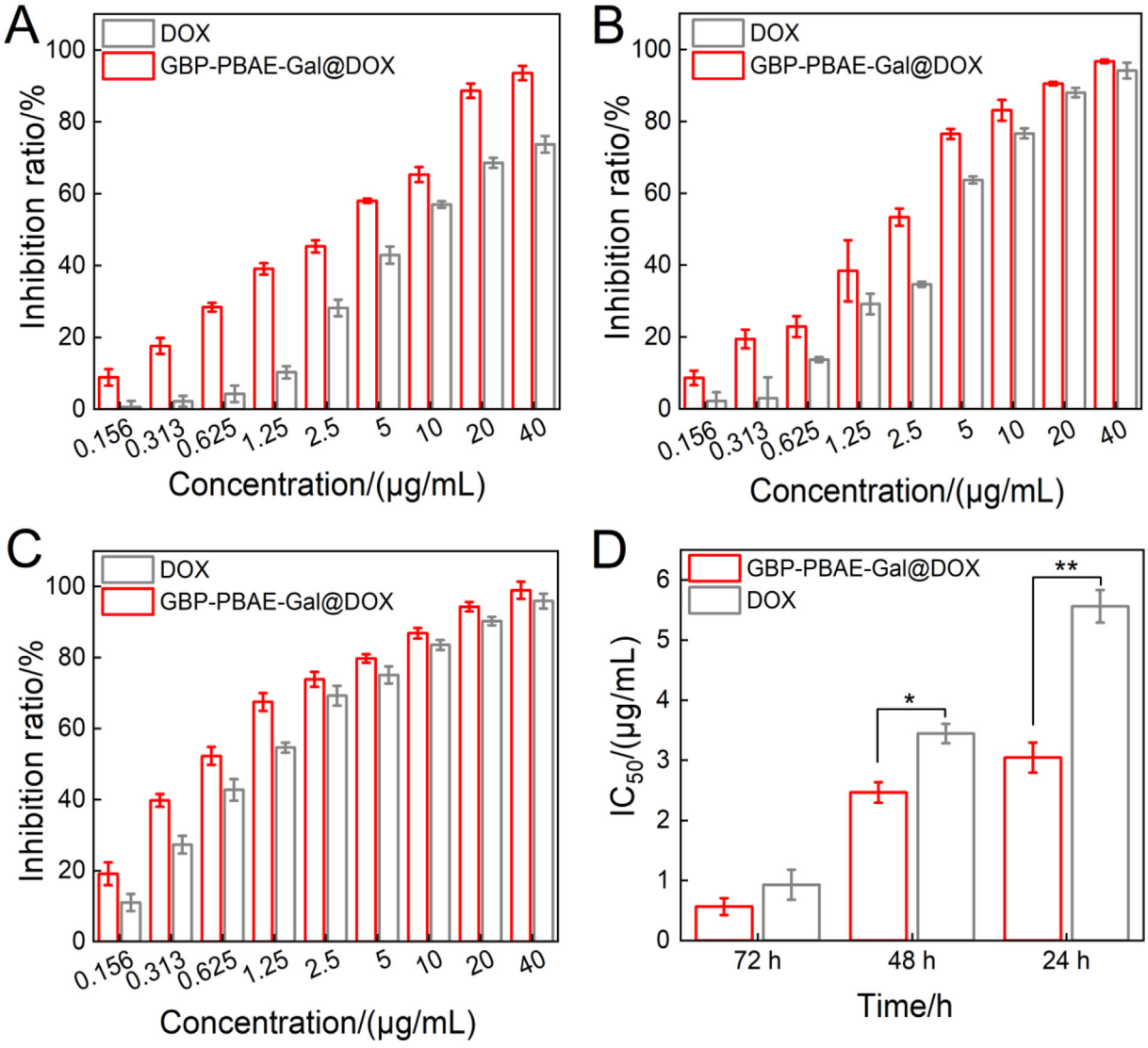

Fig. 8 In vitro cytotoxicity of GBP-PBAE-Gal@DOX micelles and free DOX at 24 h (A), 48 h (B) and 72 h (C) (mean ± SD, n = 3), and the IC_{50} of GBP-PBAE-Gal@DOX micelles and free DOX against HepG2 cells (D) (mean ± SD, n = 3). *p < 0.05, **p < 0.01.

cytocompatibility of the GBP-PBAE-Gal micelles. To sum up, the admirable biocompatibility with human normal HL-7702 cells and red blood cells confirmed the safety and applicability of GBP-PBAE-Gal as a drug carrier for anticancer drugs.

3.7. Anticancer activity

To evaluate the drug delivery performances of GBP-PBAE-Gal micelles, the anticancer activity of free DOX and GBP-PBAE-Gal@DOX micelles was studied and compared, as shown in Fig. 8. Both GBP-PBAE-Gal@DOX micelles and free DOX displayed dose-dependent cytotoxicity to HepG2 cells. In the tested dose range, a higher drug dose leads to stronger cytotoxicity with increased cell inhibition. Moreover, the cytotoxicity of GBP-PBAE-Gal@DOX micelles on HepG2 cells was significantly higher than that of free DOX at the sample DOX dose. The cell inhibition rate of free DOX at 40 μg/mL for 24 h is 78.66 ± 2.40 %, while this value enhances to 93.76 ± 1.33 % for the DOX after loading into the GBP-PBAE-Gal micelles. After incubation for 48 h and 72 h, the cell inhibition rate of GBP-PBAE-Gal@DOX micelles can be further increased to 96.31 ± 2.21 % and 98.93 ± 1.54 % (Fig. 8B and 8C). These results demonstrated that the DOX can be utilized more efficiently when delivered by GBP-PBAE-Gal@DOX micelles. This is because, on one hand, GBP-PBAE-Gal micelles improved the solubility of hydrophobic DOX for effective transportations to cancer cell surfaces (Grebinyk et al., 2022), and on the other hand, it may increase the targeted accumulation of DOX in HepG2 cells due to the targeting of GBP-PBAE-Gal micelles mediated by the galactose fragments, emerging a dose-dependent phenomenon. (Cheng et al., 2022). At the same time, the better membrane permeability of polyprenol may also facilitate the faster entry of GBP-PBAE-Gal@DOX micelles into cancer cells, accelerating the release of DOX for faster therapeutic efficacy. The half maximal inhibitory concentration (IC_{50}) of GBP-PBAE-Gal@DOX micelles and free DOX under three of incubation time was shown in Fig. 8D, the IC_{50} value of GBP-PBAE-

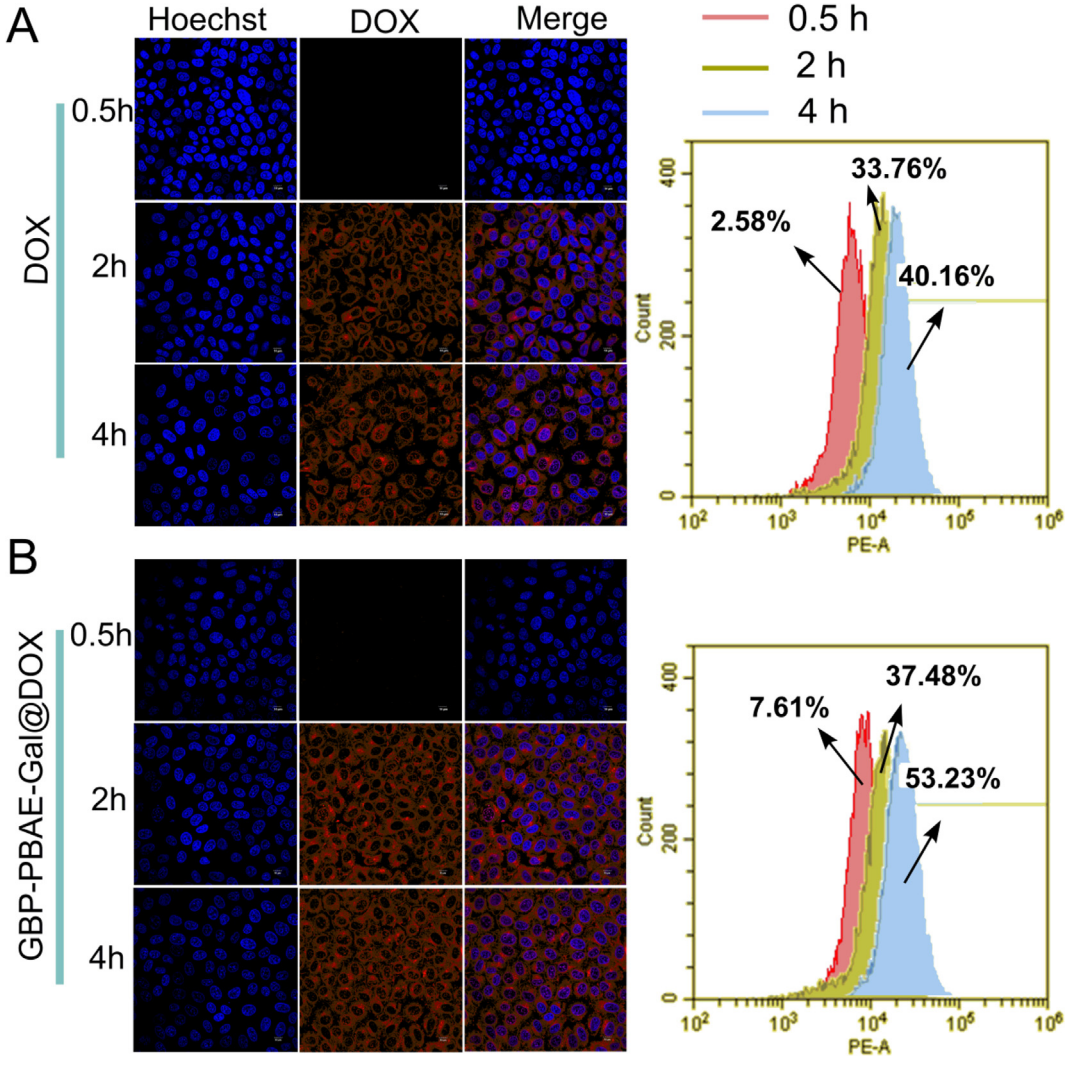

Fig. 9 Intracellular uptake of free DOX (A) and GBP-PBAE-Gal@DOX micelles (B) in HepG2 cells via the observation of confocal fluorescence microscopy and flow cytometry with incubation for 0.5, 2, and 4 h. Blue and red represent Hoechst 33,342 and DOX, respectively. Scale bars: 10 μm.

Gal@DOX micelles reached the lowest value of 0.56 μg/mL at 72 h, which is smaller than that of DOX (0.93 μg/mL), indicating that the GBP-PBAE-Gal can realize the efficient delivery and reinforce inhibition activity of DOX against HepG2 cells.

3.8. Cellular uptake

The drug efficacy depends on the efficient uptake of cells, the cell uptake of GBP-PBAE-Gal@DOX micelles and free DOX was investigated by confocal laser scanning microscopy (CLSM) and flow cytometry (FCM), as illustrated in Fig. 9. In the diagram, DOX expressed red fluorescence, the cell nucleus was blue via counterstaining with Hochest 33,342 and the merged image was shown on the right. The red fluorescence intensity increased with incubation time in the CLSM for GBP-PBAE-Gal@DOX micelles and free DOX, and the red fluorescence was primarily distributed in the cell nucleus of the tumor cells. Notably, GBP-PBAE-Gal@DOX micelles displayed a more pronounced uptake efficiency with time (Fig. 9B), which was also verified by flow cytometric quantitation of the red fluorescence intensity. After 4 h of incubation, the uptake efficiency of GBP-PBAE-Gal@DOX micelles by HepG2 cells was 53.23 %, which was higher than that of DOX (40.16 %). This result correlated with the galactose fragment in the GBP-PBAE-Gal@DOX micelles. Because galactose has a specific affinity for asialoglycoprotein receptor (ASGPR) overexpressed on HepG2 cells, the drug contained galactose fragments can integrate to ASGPR of HepG2 cells

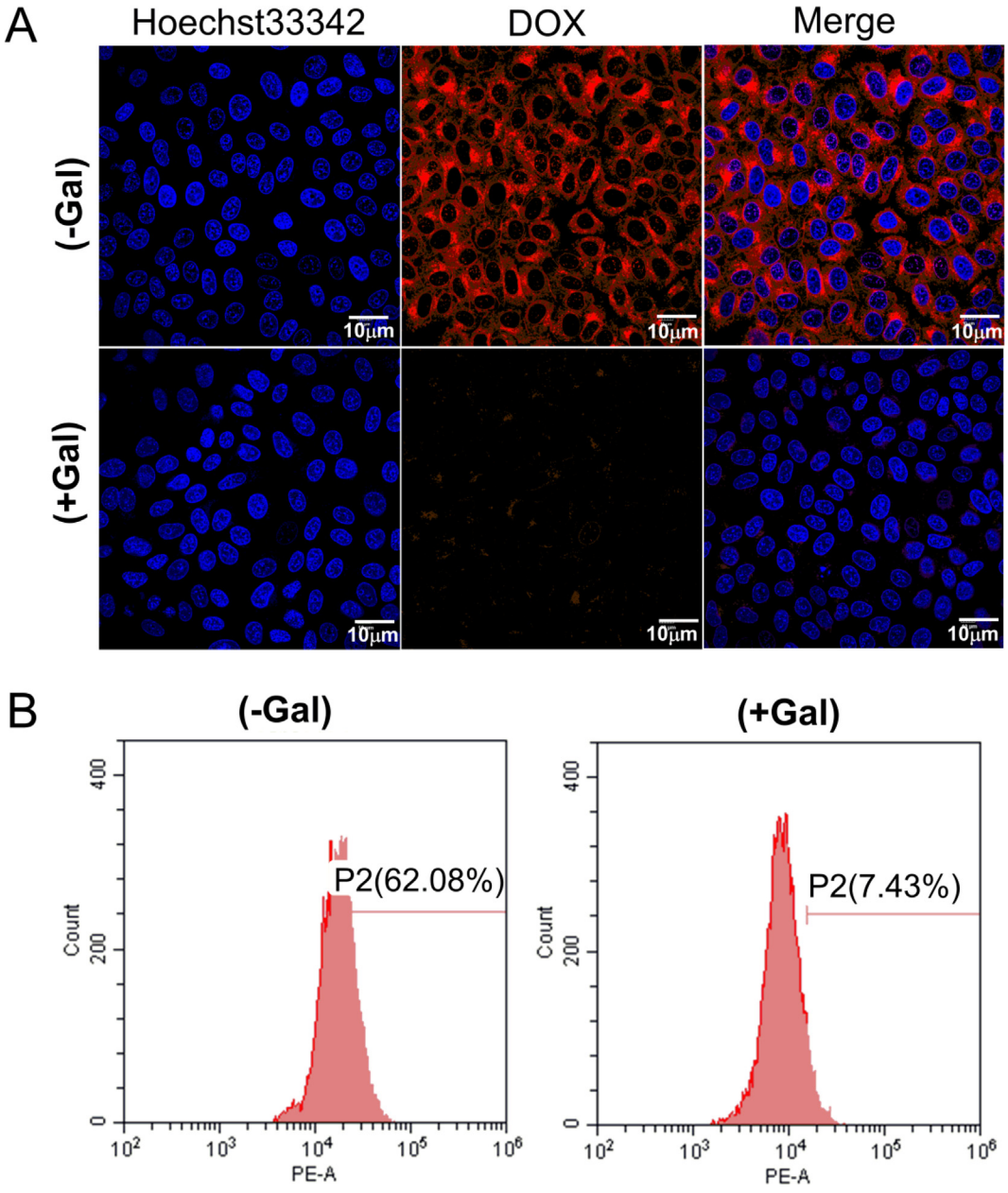

Fig. 10 Fluorescence microscopy images (A) and flow cytometric analysis (B) of HepG2 cells after culture with GBP-PBAE-Gal@DOX micelles and free DOX for 4 h with or without pre-treatment with free galactose (+Gal and -Gal). Blue and red represent Hoechst 33,342 and DOX, respectively.

to enhance targeted therapy. (Du et al., 2021). Therefore, the red fluorescence intensity of GBP-PBAE-Gal@DOX micelles in HepG2 cells is higher than that of free DOX with the power assist of galactose. Meantime, DOX was well localized to HepG2 cells via the targeted delivery of GBP-PBAE-Gal micelles.

3.9. Targeting behavior

To validate the role of galactose in facilitating cellular uptake of the micelles, HepG2 cells were preincubated with excess galactose to saturate the cellular ASGPR and further incubated with GBP-PBAE-Gal@DOX micelles. Then, DOX fluorescence intensity in HepG2 cells was qualitatively and quantitatively analyzed by CLSM and FCM, severally, as shown in Fig. 10. In the CLSM results (Fig. 10A), the intracellular red fluorescence in the receptor-saturated group (+Gal) was significantly weaker than that of the unsaturated group (-Gal). The red fluorescence intensity measured by FCM (Fig. 10B) also showed the same uptake result as that of CLSM. The uptake efficiency of GBP-PBAE-Gal@DOX micelles in the receptor-saturated group was 7.43 % and was significantly reduced by 9.0 times compared with that of the unsaturated group (62.08 %). This result is caused by the com-

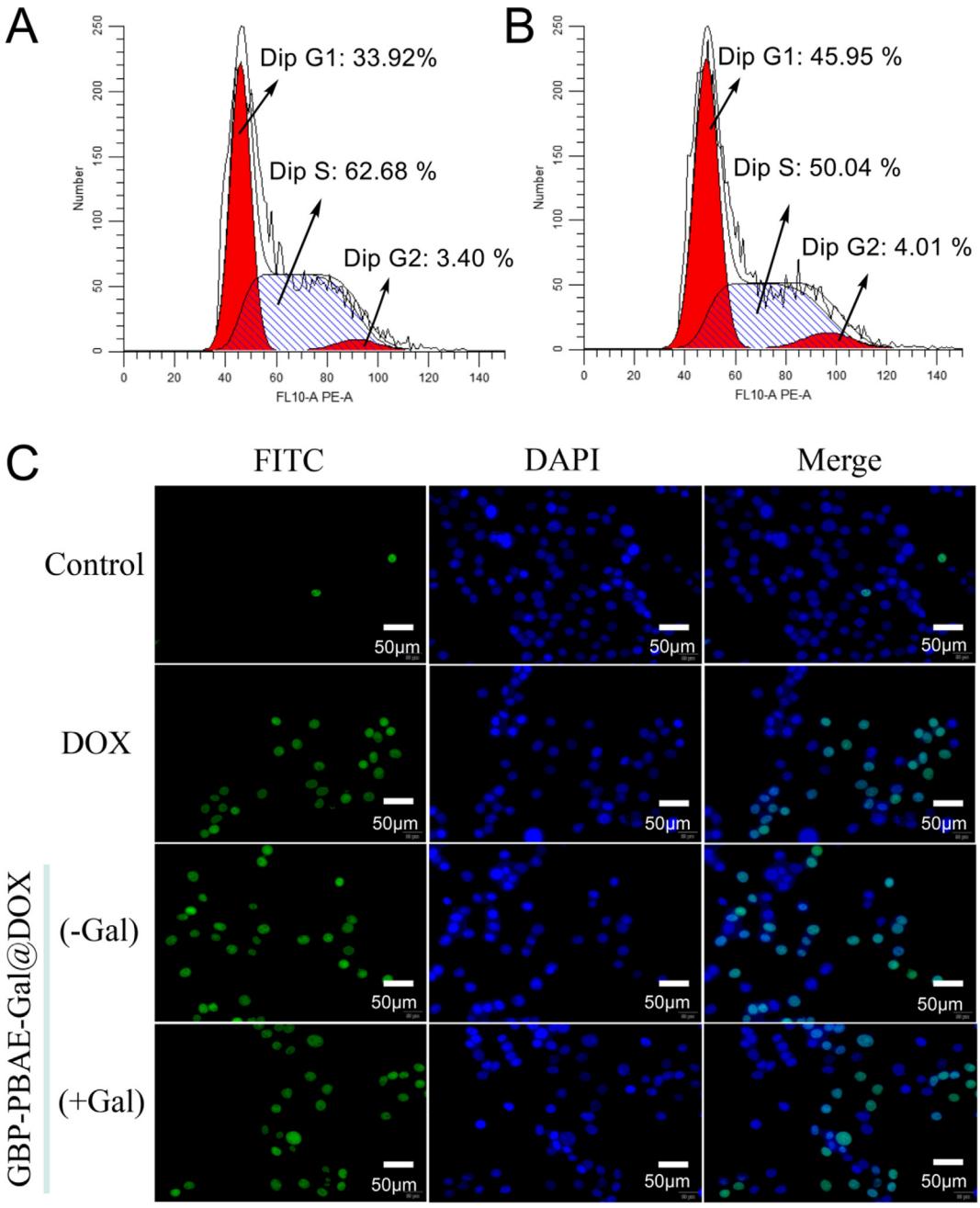

Fig. 11 The cell cycle of HepG2 cells treated with GBP-PBAE-Gal@DOX micelles (A) and free DOX (B), and the apoptosis morphology (C) of HepG2 cells treated with GBP-PBAE-Gal@DOX micelles (pre-saturated (+Gal) and unsaturated with galactose (-Gal)) and free DOX.

petitive binding of free galactose and GBP-PBAE-Gal@DOX micelles to ASGPR, which will prevent the further uptake of newly added GBP-PBAE-Gal@DOX micelles by HepG2 cells when the ASGPR was pre-saturated with excess galactose, resulting the low uptake efficiency of the receptor-saturated group (+Gal). (Tang et al., 2021). The result suggested that the GBP-PBAE-Gal@DOX micelles were dependent on the specific endocytosis mechanism of galactose, which was essential for the effective intracellular delivery of DOX for GBP-PBAE-Gal micelles. In summary, GBP-PBAE-Gal@DOX micelles could target HepG2 cells and realize the effective delivery and accumulation of DOX in HepG2 cells.

3.10. Cell cycle and apoptosis

It is of great significance to study the regulation mechanism of drugs on the cell cycle for cancer treatment. So, the cell cycle of HepG2 cells treated with GBP-PBAE-Gal@DOX micelles was determined, as shown in Fig. 11A. DOX can insert into the DNA of anticancer cells and inactivate both DNA and RNA polymerase to inhibit DNA replication and RNA transcription (S phase), thereby cell growth is inhibited in S-phase once DOX exerts its antitumor effects. (Wang et al., 2022). It can be seen that both GBP-PBAE-Gal@DOX micelles and free DOX can arrest cells in S-phase, reflecting that the DOX loaded into GBP-PBAE-Gal micelles had comparable antitumor efficacy with free DOX. In addition, the GBP-PBAE-Gal@DOX micelles were more potent in arresting cells in S-phase compared to free DOX, with a 62.68 % arresting rate of S-phase cells. Taking the result of cellular uptake and in vitro cytotoxicity into account, this phenomenon may be explained by the targeting properties of GBP-PBAE-Gal@DOX micelles to HepG2 cells and their pH/GSH-response properties for efficient DOX release. Besides, the presence of GBP-PBAE-Gal decreased the percentage of cells arrested in the DNA pre-synthetic phase (G1 phase) in contrast to free DOX, indicating that GBP-PBAE-Gal@DOX micelles were more effective in anti-cancer activity against HepG2 cells. G1 phase is the restriction point for cells to complete a cycle, in that it prepares the substance and energy for the next stage of DNA replication (S phase), and reducing the percentage of cells in this phase will be key for controlling cell proliferation (Yang et al., 2021). Therefore, GBP-PBAE-Gal micelles increased the sensitivity of G1-stage cancer cells to DOX and induced them to enter the cell cycle, which had a potent contribution for DOX to further kill HepG2 cells.

The ability of cancer cells to proliferate indefinitely lies in the ability to circumvent the apoptotic phase of cell death. To further clarify the pro-apoptotic effect of GBP-PBAE-Gal@DOX micelles on HepG2 cells, cell apoptosis was detected by the TUNEL method and western blotting method. As shown in Fig. 11C, the majority of HepG2 cells were in good condition with a few necrotic cells in the negative control group without any drugs, and this result was also confirmed by the results of cell nuclear staining with DAPI, which showed a normal shuttle shape with a clear background for HepG2 cells. In the GBP-PBAE-Gal@DOX group, the apoptotic number of HepG2 cells without pre-saturation of galactose was significantly increased and a severe apoptotic morphology was observed: the nuclei of HepG2 cells were fragmented into punctate shapes and appeared a large number of apoptotic vesicles. In the DOX group, the morphology of HepG2 cells was shrivel and rounded with the distorted cell membrane. Furthermore, it is seen from the apoptosis rate of HepG2 cells in each group (Fig. S8), the apoptosis result was in the order of GBP-PBAE-Gal@DOX (-Gal) > GBP-PBAE-Gal@DOX (+Gal) > DOX. GBP-PBAE-Gal@DOX (-Gal) exhibited a higher apoptosis rate of 58.06 % than free DOX at 24 h, revealing the powerful anticancer activity of GBP-PBAE-Gal@DOX micelles than that of free DOX, which was profited from the targeting function of GBP-PBAE-Gal on HepG2 cells (Tang et al., 2021). Meanwhile, the low apoptosis rate of HepG2 cells in the GBP-PBAE-Gal@DOX (+Gal) group further confirmed the fact that the pre-saturation of HepG2 cells with galactose was indeed hindering the further uptake of GBP-PBAE-Gal@DOX micelles by HepG2 cells, thus leading to their slightly weaker inhibiting effect against cancer cells.

4. Conclusion

A *Ginkgo biloba* leaves polyprenol-based derivative (GBP-PBAE-Gal) was synthesized by Michael addition reaction of poly (β-amino esters) with *Ginkgo biloba* leaves polyprenol and galactose. As a result of the introduction of galactose and PBAE into the structure of Ginkgo biloba leaves polyprenol, the newly designed GBP-PBAE-Gal can self-assemble into micelles in an aqueous solution to act as a drug carrier to load DOX by hydrophobic interaction, with the highest loading of 28.62 ± 1.49 %. GBP-PBAE-Gal carrier could achieve a high degree of colloidal stability in 640 times of dilutions up and in the presence of blood. Moreover, the GBP-PBAE-Gal carrier achieved long-term storage stability at room temperature. The GBP-PBAE-Gal carrier was triggered by its pH and GSH response in a specific tumor microenvironment to realize the controlled release of DOX, which is attributed to the proton sponge effect of PBAE blocks and the breakage of disulfide bonds in GBP-PBAE-Gal carrier in a co-environment of acidic pH and high GSH. The maximum cumulative release of DOX was 90.30 % at 24 h. GBP-PBAE-Gal carrier was safe for both human red blood cells and normal HL-7702 cells, displaying favorable reliability when applied as a carrier for drug delivery. Meantime, the DOX loaded into GBP-PBAE-Gal carrier possessed enhanced anticancer activity against HepG2 cells than that of free DOX, with the smallest IC_{50} value of 0.56 μg/mL after 72 h of incubation with HepG2 cells, which is due to the pH/GSH-responsive release of GBP-PBAE-Gal and targeting delivery mediated by galactose. Besides, the anticancer mechanism studies revealed that GBP-PBAE-Gal carrier has a synergistic effect during DOX blockade of the DNA synthesis phase (s-phase) in HepG2 cells. This work presents the idea of GBP-based derivatives as new delivery components for poorly water-soluble drug delivery and confirms their great promise in delivering drugs and enhancing therapy, providing a new candidate for the biological delivery system.

CRediT authorship contribution statement

Hua Yuan: Conceptualization, Methodology, Data curation, Writing – original draft. **Changwei Zhang:** Funding acquisition, Writing – review & editing. **Peng Zhou:** Resources, Software. **Xiaoran Yang:** Resources, Software. **Ran Tao:** Methodology. **Jianzhong Ye:** Resources, Software. **Chengzhang Wang:** Funding acquisition, Writing – review & editing, Supervision.

Declaration of Competing Interest

The authors declare that they have no known competing financial interests or personal relationships that could have appeared to influence the work reported in this paper.

Acknowledgments

The work was supported by Fundamental Research Funds of Research Institute of Forest New Technology, CAF (CAFYBB2020SY039) and National Natural Science Foundation of China (32101473).

Appendix A. Supplementary material

Supplementary data to this article can be found online at https://doi.org/10.1016/j.arabjc.2023.104679.

References

Aapro, M., Caprariu, Z., Chilingirov, P., et al, 2022. Assessing the impact of antiemetic guideline compliance on prevention of chemotherapy-induced nausea and vomiting: results of the nausea/emesis registry in oncology (NERO). Eur. J. Cancer 166, 126–133. https://doi.org/10.1016/j.ejca.2022.01.028.

Arafa, K.K., Hamzawy, M.A., Mousa, S.A., et al, 2022. Mitochondria-targeted alginate/triphenylphosphonium-grafted-chitosan for treatment of hepatocellular carcinoma. RSC Adv. 12, 21690–21703. https://doi.org/10.1039/d2ra03240f.

Blayney, D.W., Schwartzberg, L., 2022. Chemotherapy-induced neutropenia and emerging agents for prevention and treatment: a review. Cancer Treat. Rev. 109,. https://doi.org/10.1016/j.ctrv.2022.102427 102427.

Boateng, I.D., Soetanto, D.A., Li, F., et al, 2021. Separation and purification of polyprenols from Ginkgo biloba L. leaves by bulk ionic liquid membrane and optimizing parameters. Industrial Crops Prod. 170,. https://doi.org/10.1016/j.indcrop.2021.113828 113828.

Calori, I.R., Caetano, W., Tedesco, A.C., et al, 2020. Determination of critical micelle temperature of Pluronic® in Pluronic/gel phase liposome mixtures using steady-state anisotropy. J. Mol. Liq. 304. https://doi.org/10.1016/j.molliq.2020.112784.

Chaudhuri, S., Fowler, M.J., Baker, C., et al, 2021. beta-Cyclodextrin-poly (beta-Amino Ester) nanoparticles are a generalizable strategy for high loading and sustained release of HDAC inhibitors. ACS Appl. Mater. Interfaces 13, 20960–20973. https://doi.org/10.1021/acsami.0c22587.

Chen, W., Liu, P., 2022. Facile synthesis of PEGylated dendritic polyurethane as unimolecular micelles for ultrasound-triggered localized drug delivery. Polym. Chem. 13, 80–84. https://doi.org/10.1039/d1py01489g.

Chen, C., Wu, C., Yu, J., et al, 2022. Photodynamic-based combinatorial cancer therapy strategies: tuning the properties of nanoplatform according to oncotherapy needs. Coord. Chem. Rev. 461. https://doi.org/10.1016/j.ccr.2022.214495.

Cheng, Y., Han, Y., Zhang, W., et al, 2022. Gram-scale synthesis of boron nitride nanosheets by salt-template method for anticancer drug delivery. Chem. Eng. J. 437. https://doi.org/10.1016/j.cej.2022.135304.

Chiaregato, C.G., Faez, R., 2021. Micronutrients encapsulation by starch as an enhanced efficiency fertilizer. Carbohydr. Polym. 271,. https://doi.org/10.1016/j.carbpol.2021.118419 118419.

Dehcheshmeh, M.A., Fathi, M., 2019. Production of core-shell nanofibers from zein and tragacanth for encapsulation of saffron extract. Int. J. Biol. Macromol. 122, 272–279. https://doi.org/10.1016/j.ijbiomac.2018.10.176.

Du, Z., Mao, Y., Zhang, P., et al, 2021. TPGS-galactose-modified polydopamine co-delivery nanoparticles of nitric oxide donor and doxorubicin for targeted chemo-photothermal therapy against drug-resistant hepatocellular carcinoma. ACS Appl. Mater. Interfaces 13, 35518–35532. https://doi.org/10.1021/acsami.1c09610.

Edueng, K., Kabedev, A., Ekdahl, A., et al, 2022. Pharmaceutical profiling and molecular dynamics simulations reveal crystallization effects in amorphous formulations. Int. J. Pharm. 613,. https://doi.org/10.1016/j.ijpharm.2021.121360 121360.

Gawrys, O., Polkowska, M., Roszkowska-Chojecka, M., et al, 2014. Effects of liposomes with polyisoprenoids, potential drug carriers, on the cardiovascular and excretory system in rats. Pharmacol. Rep. 66, 273–278. https://doi.org/10.1016/j.pharep.2013.09.009.

Gawrys, O., Baranowska, I., Gawarecka, K., et al, 2018. Innovative lipid-based carriers containing cationic derivatives of polyisoprenoid alcohols augment the antihypertensive effectiveness of candesartan in spontaneously hypertensive rats. Hypertens. Res. 41, 234–245. https://doi.org/10.1038/s41440-018-0011-y.

Gawrys, O., Rak, M., Baranowska, I., et al, 2021. Polyprenol-based lipofecting agents for in vivo delivery of therapeutic DNA to treat hypertensive rats. Biochem. Genet. 59, 62–82. https://doi.org/10.1007/s10528-020-09992-9.

Grebinyk, A., Prylutska, S., Grebinyk, S., et al, 2022. Drug delivery with a pH-sensitive star-like dextran-graft polyacrylamide copolymer. Nanoscale Adv. 4, 5077–5088. https://doi.org/10.1039/d2na00353h.

Grecka, E., Statkiewicz, M., Gorska, A., et al, 2016. Prenyl ammonium salts-new carriers for gene delivery: a B16–F10 mouse melanoma model. PLoS One 11, e0153633. https://doi.org/10.1371/journal.pone.0153633.

Guo, Y., Wang, M., Gao, C., et al, 2021. Spatial prediction and delineation of Ginkgo biloba production areas under current and future climatic conditions. Industrial Crops Prod. 166. https://doi.org/10.1016/j.indcrop.2021.113444.

Guo, Q., Zhang, L., He, M., et al, 2021. Doxorubicin-loaded natural daptomycin micelles with enhanced targeting and anti-tumor effect in vivo. Eur. J. Med. Chem. 222,. https://doi.org/10.1016/j.ejmech.2021.113582 113582.

Jansone, B., Dzirkale, Z., Jekabsons, K., et al, 2016. Spruce needle polyprenols protect against atorvastatin-induced muscle weakness and do not influence central nervous system functions in rats. Nephron Clin. Pract. 70, 13–20. https://doi.org/10.1515/prolas-2016-0003.

Li, M., Zhao, Y., Sun, J., et al, 2022. pH/reduction dual-responsive hyaluronic acid-podophyllotoxin prodrug micelles for tumor targeted delivery. Carbohydr. Polym. 288,. https://doi.org/10.1016/j.carbpol.2022.119402 119402.

Lichota, A., Gwozdzinski, L., Gwozdzinski, K., 2019. Therapeutic potential of natural compounds in inflammation and chronic venous insufficiency. Eur. J. Med. Chem. 176, 68–91. https://doi.org/10.1016/j.ejmech.2019.04.075.

Lin, C., Liang, Y., Guo, M., et al, 2022. Stimuli-responsive polyprodrug for cancer therapy. Mater. Today Adv. 15. https://doi.org/10.1016/j.mtadv.2022.100266.

Liu, H., Hu, Z., Chen, H., et al, 2022. Self-degradable poly(beta-amino ester)s promote endosomal escape of antigen and agonist. J. Control. Release 345, 91–100. https://doi.org/10.1016/j.jconrel.2022.03.006.

Mahdavi, B., Hosseini, S., Mohammadhosseini, M., et al, 2022. Preparation and characterization of a novel magnetized nanosphere as a carrier system for drug delivery using Plantago ovata Forssk. hydrogel combined with mefenamic acid as the drug model. Arab. J. Chem. 15. https://doi.org/10.1016/j.arabjc.2022.104128.

Mennati, A., Rostamizadeh, K., Manjili, H.K., et al, 2022. Co-delivery of siRNA and lycopene encapsulated hybrid lipid nanoparticles for

dual silencing of insulin-like growth factor 1 receptor in MCF-7 breast cancer cell line. Int. J. Biol. Macromol. 200, 335–349. https://doi.org/10.1016/j.ijbiomac.2021.12.197.

Muceniece, R., Namniece, J., Nakurte, I., et al, 2016. Pharmacological research on natural substances in Latvia: Focus on lunasin, betulin, polyprenol and phlorizin. Pharmacol. Res. 113, 760–770. https://doi.org/10.1016/j.phrs.2016.03.040.

Park, C., Lim, J.W., Park, G., et al, 2021. Kinetic stability modulation of polymeric nanoparticles for enhanced detection of influenza virus via penetration of viral fusion peptides. J. Mater. Chem. B 9, 9658–9669. https://doi.org/10.1039/d1tb01847g.

Peppas, N.A., 2014. 1. commentary on an exponential model for the analysis of drug delivery. J. Control. Release 190, 31–32. https://doi.org/10.1016/s0168-3659(14)00482-9.

N.A. Peppas, J. J. S., 1989. A simple equation for the description of solute release. III. Coupling of diffusion and relaxation. Int. J. Pharm. 57 169-172

Pronin, A.V., Narovlyansky, A.N., Sanin, A.V., 2021. New approaches to the prevention and treatment of viral diseases. Arch. Immunol. Ther. Exp. (Warsz). 69, 10. https://doi.org/10.1007/s00005-021-00613-w.

Qiu, L., Xu, J., Ahmed, K.S., et al, 2022. Stimuli-responsive, dual-function prodrug encapsulated in hyaluronic acid micelles to overcome doxorubicin resistance. Acta Biomater. 140, 686–699. https://doi.org/10.1016/j.actbio.2021.11.050.

Rak, M., Ochalek, A., Gawarecka, K., et al, 2020. Boost of serum resistance and storage stability in cationic polyprenyl-based lipofection by helper lipids compositions. Eur. J. Pharm. Biopharm. 155, 199–209. https://doi.org/10.1016/j.ejpb.2020.07.028.

Ren, X., Wang, N., Zhou, Y., et al, 2021. An injectable hydrogel using an immunomodulating gelator for amplified tumor immunotherapy by blocking the arginase pathway. Acta Biomater. 124, 179–190. https://doi.org/10.1016/j.actbio.2021.01.041.

Y. Rui , D. R. W., S. Y. Tzeng , H. M. Yamagata, D. Sudhakar, M. Conge, C. A. Berlinicke, D. J. Zack. A. Tuesca, J. J. Green., 2022. High-throughput and high-content bioassay enables tuning of polyester nanoparticles for cellular uptake, endosomal escape, and systemic in vivo delivery of mRNA. Sci Adv. 8, eabk2855.

Sahkulubey Kahveci, E.L., Kahveci, M.U., Celebi, A., et al, 2022. Glycopolymer and poly(beta-amino ester)-based amphiphilic block copolymer as a drug carrier. Biomacromolecules 23, 4896–4908. https://doi.org/10.1021/acs.biomac.2c01076.

Sharma, R., Porterfield, J.E., An, H.T., et al, 2021. Rationally designed galactose dendrimer for hepatocyte-specific targeting and intracellular drug delivery for the treatment of liver disorders. Biomacromolecules 22, 3574–3589. https://doi.org/10.1021/acs.biomac.1c00649.

Shehata, E.M.M., Gowayed, M.A., El-Ganainy, S.O., et al, 2022. Pectin coated nanostructured lipid carriers for targeted piperine delivery to hepatocellular carcinoma. Int. J. Pharm. 619,. https://doi.org/10.1016/j.ijpharm.2022.121712 121712.

Shukla, S.K., Sarode, A., Wang, X., et al, 2022. Particle shape engineering for improving safety and efficacy of doxorubicin - a case study of rod-shaped carriers in resistant small cell lung cancer. Biomater. Adv. 137,. https://doi.org/10.1016/j.bioadv.2022.212850 212850.

Surya, R., Mullassery, M.D., Fernandez, N.B., et al, 2020. Synthesis and characterization of a pH responsive and mucoadhesive drug delivery system for the controlled release application of anti-cancerous drug. Arab. J. Chem. 13, 5262–5276. https://doi.org/10.1016/j.arabjc.2020.03.005.

Tang, Y., Tang, Z., Li, P., et al, 2021. Precise Delivery of Nanomedicines to M2 macrophages by combining "Eat Me/Don't Eat Me" signals and its anticancer application. ACS Nano 15, 18100–18112. https://doi.org/10.1021/acsnano.1c06707.

Tao, R., Wang, C., Ye, J., et al, 2016. Polyprenols of Ginkgo biloba enhance antibacterial activity of five classes of antibiotics. Biomed. Res. Int. 2016, 4191938. https://doi.org/10.1155/2016/4191938.

van der Vlies, A.J., Xu, J., Ghasemi, M., et al, 2022. Thioether-based polymeric micelles with fine-tuned oxidation sensitivities for chemotherapeutic drug delivery. Biomacromolecules 23, 77–88. https://doi.org/10.1021/acs.biomac.1c01010.

Van Gelder, K., Virta, L.K.A., Easlick, J., et al, 2021. A central role for polyprenol reductase in plant dolichol biosynthesis. Plant Sci. 303,. https://doi.org/10.1016/j.plantsci.2020.110773 110773.

Vanaga, I., Gubernator, J., Nakurte, I., et al, 2020. Identification of Abies sibirica L. polyprenols and characterisation of polyprenol-containing liposomes. Molecules 25, 1801. https://doi.org/10.3390/molecules25081801.

Wang, Z., Ding, B., Zhao, Y., et al, 2022. Tumor-oriented mathematical models in hydrogel regulation for precise topical administration regimens. J. Control. Release 345, 610–624. https://doi.org/10.1016/j.jconrel.2022.03.042.

Wang, Y., Hou, M., Duan, S., et al, 2022. Macrophage-targeting gene silencing orchestrates myocardial microenvironment remodeling toward the anti-inflammatory treatment of ischemia-reperfusion (IR) injury. Bioact. Mater. 17, 320–333. https://doi.org/10.1016/j.bioactmat.2022.01.026.

Wang, C.Z., Li, W.J., Tao, R., et al, 2015. Antiviral activity of a nanoemulsion of polyprenols from ginkgo leaves against influenza A H3N2 and hepatitis B virus in vitro. Molecules 20, 5137–5151. https://doi.org/10.3390/molecules20035137.

Yang, L., Wang, C.Z., Ye, J.Z., et al, 2011. Hepatoprotective effects of polyprenols from Ginkgo biloba L. leaves on CCl4-induced hepatotoxicity in rats. Fitoterapia 82, 834–840. https://doi.org/10.1016/j.fitote.2011.04.009.

Yang, L., Cao, J., Wei, J., et al, 2021. Antiproliferative activity of berberine in HepG2 cells via inducing apoptosis and arresting cell cycle. Food Funct. 12, 12115–12126. https://doi.org/10.1039/d1fo02783b.

Zhan, Y.R., Tan, J., Hei, M.W., et al, 2022. Construction of GSH-triggered cationic fluoropolymers as two-in-one nanoplatforms for combined chemo-gene therapy. J. Mater. Chem. B 10, 1308–1318. https://doi.org/10.1039/d1tb02602j.

Zhang, C.-W., Li, M.-F., Tao, R., et al, 2020. Physiochemical property and antibacterial activity of formulation containing polyprenol extracted from Ginkgo biloba leaves. Industrial Crops Prod. 147,. https://doi.org/10.1016/j.indcrop.2020.112213 112213.

Zhang, M., Li, S., Peng, J., et al, 2022. Multivalent cyclic template-directed synthesis of polycyclodextrin-based nanocarriers for enhanced chemotherapy. Mater. Today Chem. 26. https://doi.org/10.1016/j.mtchem.2022.100996.

Zhang, M., Qin, X., Zhao, Z., et al, 2022. A self-amplifying nanodrug to manipulate the Janus-faced nature of ferroptosis for tumor therapy. Nanoscale Horiz. 7, 198–210. https://doi.org/10.1039/d1nh00506e.

Zhang, C.W., Wang, C.Z., Tao, R., et al, 2019. Separation of polyprenols from Ginkgo biloba leaves by a nano silica-based adsorbent containing silver ions. J. Chromatogr. A 1590, 58–64. https://doi.org/10.1016/j.chroma.2019.01.047.

Zhang, M., Yu, H., Hu, J., et al, 2022. Therapeutic carrier based on solanesol and hyaluronate for synergistic tumor treatment. Int. J. Biol. Macromol. 201, 20–28. https://doi.org/10.1016/j.ijbiomac.2021.12.194.

Zhou, S., Shang, Q., Wang, N., et al, 2020. Rational design of a minimalist nanoplatform to maximize immunotherapeutic efficacy: Four birds with one stone. J. Control. Release 328, 617–630. https://doi.org/10.1016/j.jconrel.2020.09.035.